nature nanotechnology

Letter

https://doi.org/10.1038/s41565-022-01219-9

Atmospheric emission of nanoplastics from sewer pipe repairs

Received: 14 December 2021

Accepted: 22 August 2022

Published online: 6 October 2022

Check for updates

Ana C. Morales[1], Jay M. Tomlin[1], Christopher P. West[1], Felipe A. Rivera-Adorno[1], Brianna N. Peterson[1], Steven A. L. Sharpe[1], Yoorae Noh[2], Seyedeh M. T. Sendesi[2], Brandon E. Boor[2], John A. Howarter[3], Ryan C. Moffet[4], Swarup China[5], Brian T. O'Callahan[6], Patrick Z. El-Khoury[5], Andrew J. Whelton[2,7] and Alexander Laskin[1] ✉

Nanoplastic particles are inadequately characterized environmental pollutants that have adverse effects on aquatic and atmospheric systems, causing detrimental effects to human health through inhalation, ingestion and skin penetration[1–3]. At present, it is explicitly assumed that environmental nanoplastics (EnvNPs) are weathering fragments of microplastic or larger plastic debris that have been discharged into terrestrial and aquatic environments, while atmospheric EnvNPs are attributed solely to aerosolization by wind and other mechanical forces. However, the sources and emissions of unintended EnvNPs are poorly understood and are therefore largely unaccounted for in various risk assessments[4]. Here we show that large quantities of EnvNPs may be directly emitted into the atmosphere as steam-laden waste components discharged from a technology commonly used to repair sewer pipes in urban areas. A comprehensive chemical analysis of the discharged waste condensate has revealed the abundant presence of insoluble colloids, which after drying form solid organic particles with a composition and viscosity consistent with EnvNPs. We suggest that airborne emissions of EnvNPs from these globally used sewer repair practices may be prevalent in highly populated urban areas[5], and may have important implications for air quality and toxicological levels that need to be mitigated.

Environmental pollution by the degradation products of plastic materials is an emerging worldwide concern, with the majority of studies focusing on the occurrence, fate and effects of micro- and nanoplastics in marine and terrestrial environments[6–9]. At present, it is assumed that microplastics enter the environment as a result of the fragmentation of large plastic objects and synthetic textiles through photochemical, biotic and abiotic degradation processes, and by the direct emission of engineered nanometre-to-micrometre size plastic beads, such as those commonly used in cosmetic products. The continuing degradation of microplastic beads (<5 mm) and fragments results in additional nanoscale plastics (<1 μm), which increases the diversity of environmental nanoplastics (EnvNPs)[4]. EnvNPs are considered a unique class of pollutants that can be distinguished from both microplastics and engineered nanoparticles through their unique physical properties and chemical composition[4]. Because of their very small size and low degradation rate, EnvNPs pose threats to ecosystems[6,10] and

[1]Department of Chemistry, Purdue University, West Lafayette, IN, USA. [2]Lyles School of Civil Engineering, Purdue University, West Lafayette, IN, USA. [3]School of Materials Engineering, Purdue University, West Lafayette, IN, USA. [4]Sonoma Technology, Petaluma, CA, USA. [5]Physical Sciences Division, Pacific Northwest National Laboratory, Richland, WA, USA. [6]Environmental Molecular Sciences Laboratory, Pacific Northwest National Laboratory, Richland, WA, USA. [7]Department of Environmental and Ecological Engineering, Purdue University, West Lafayette, IN, USA. ✉e-mail: alaskin@purdue.edu

https://doi.org/10.1038/s41565-022-01219-9

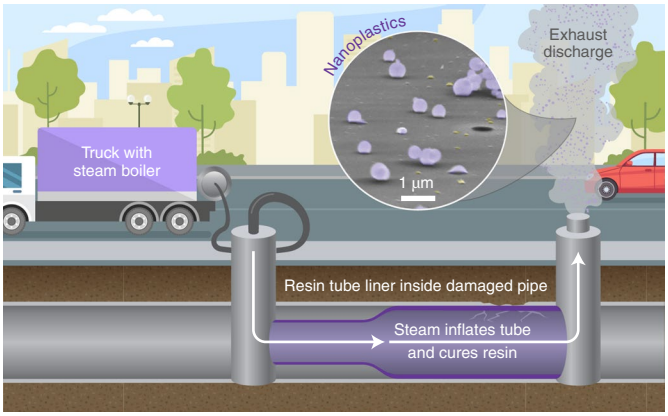

Fig. 1 | A schematic illustration of CIPP installation. A flexible resin-impregnated tube is first inserted into the damaged pipe. This tube is inflated against the damaged pipe wall by pumping ambient air, water and/or steam through the tube. Next, the tube is cured in place using either thermal (hot steam injected into the tube) or ultraviolet curing methods, and the waste is discharged into the environment. After curing, the newly installed plastic pipe is cooled by blowing forced ambient air through the tube, also resulting in the atmospheric discharge of waste laden with EnvNP particles.

are also considered of immediate (acute) toxicological concern as a result of direct inhalation and deposition in lungs[4]. Long-term (chronic) toxicological effects also occur through their bioaccumulation in food chains, which eventually leads to ingestion by humans, posing additional threats to human health[2,3,11]. Compared with the plethora of studies of microplastics in marine and terrestrial environments, reports on EnvNP particles, especially their airborne occurrences, are scarce. The observations reported here challenge our understanding of EnvNP formation and suggest that common municipal practices of sewer pipe repairs constitute a direct atmospheric emission source.

The cured-in-place-pipe (CIPP) installation of plastic pipes is the most popular, least expensive and most frequently used technology used to cure leaking sanitary and stormwater sewers through the insertion of new plastic pipes inside the existing pipes (Fig. 1)[5]. Waste plumes discharged during CIPP manufacture are complex multiphase mixtures of volatile and semi-volatile organic compounds (VOC and SVOC, respectively), primary and secondary organic aerosols, and the fine debris of partially cured resin, all blown into the atmosphere at substantial concentrations at worksites (Supplementary Video 1). Specifically, detected VOCs are reported[12–14] to be at the level of 394–757 parts per million by volume, which is four to five orders of magnitude higher than the background VOC concentrations (<100 ppb) reported even in heavily polluted urban areas[15]. While dispersion model analysis and field measurements show notable dilution of the VOC concentrations down to sub-parts per million levels at distances of ~50 m downwind, local instances of degraded air quality have affected both indoor and outdoor environments in urban neighbourhoods and even prompted building evacuations[13,16]. Furthermore, recent field measurements[16,17] have shown that additional condensed-phase organic pollutants are also emitted into the atmosphere around CIPP installation sites, although their qualitative and quantitative characteristics are as yet largely unknown.

Analysis of the discharged waste condensate collected at four CIPP operation sites (labelled X1, X2, X4 and X5 in Supplementary Note 1) revealed the abundant presence of colloidal material; this colloidal material forms airborne particles as water evaporates from microdroplets of the discharged waste. An array of complementary analytical measurements were used for the systematic characterization of both the colloidal material and the resulting dry particles (Supplementary Note 2). Figure 2 illustrates the particle mass size distributions of both the wet colloids detected in the condensate samples (Supplementary Note 3) and the aerosolized dry particles generated from the same samples (Supplementary Note 4). In all four samples, the sizes of the wet colloids and dry particles are in the submicrometre range: the mean sizes of the wet colloids and dry particles are ~1 and ~0.5 µm, respectively. The submicrometre particles remain airborne for days to weeks[18], and therefore they need to be viewed as air pollutants emitted at CIPP installation sites. Quantitative assessment of the mass loadings of the condensed-phase organic material emitted as dry aerosol particles per litre of discharged waste condensate revealed values of between 0.01 and 3.24 mg l^{-1} for the four reported samples (Supplementary Note 4). The highest mass loading of 1.65–3.24 mg l^{-1} was estimated for the CIPP installation site X1, where the highest concentrations of gas-phase styrene (well-known polymerization component) were evident (Supplementary Table 1). This correlation between high levels of emitted styrene and particulates strongly suggests that the chemical composition of the dry particles is likely to show a close resemblance to the polymeric structure of the nanoplastics. Furthermore, molecular analysis of the solvent-dissolved components of the CIPP condensate from the X1 site showed a very complex mixture of chemical pollutants that can polymerize and partition between gaseous, aqueous and solid phases when water evaporates from the discharged steam-laden waste. Chemical characterization of this mixture using liquid chromatography coupled to photodiode array and high-resolution mass detectors uncovered a wide range of molecular components with a broad variation in molecular weight, structure and degree of oxidation (Supplementary Note 5). Many of the identified compounds were polymer precursors and initiators, plausibly washed out from the surface of the uncured resin tube. Among them are various hazardous air pollutants (phenol, dibutyl phthalate and styrene) controlled by the US Environmental Protection Agency[19], known and suspected carcinogens (styrene, benzo[*ghi*]perylene and pyrene)[20], endocrine-disrupting compounds (dibutyl phthalate and styrene)[21] and compounds with little toxicity data (bis(4-*tert*-butylcyclohexyl) peroxydicarbonate). The detection of polymer precursors and various low-volatility components in these mixtures prompts the hypothesis that the evaporation of water from microdroplets of discharged waste would result in the solidification of dry particles, and that their chemical composition and physical properties would resemble EnvNPs[4]. A mechanism describing the peroxide-initiated radical polymerization of CIPP monomer styrene is illustrated in Supplementary Scheme 1 in Supplementary Note 6. However, it is also plausible that common environmental aqueous-phase oligomerization reactions[22–28] (Supplementary Scheme 2) will concurrently occur in the drying microdroplets, producing solid EnvNPs with variable composition.

Consistent with this hypothesis, spectromicroscopic analysis of the chemical composition, viscoelastic properties and internal and external mixing states of the dry particles generated from the waste condensate samples showed that their characteristics are very much consistent with EnvNPs. Figure 3a shows a representative scanning electron microscopy (SEM) image, acquired at a tilt angle of 75°, of dry particles generated from the X1 sample, deposited on an impactor substrate. Upon impact with the substrate, the particles deform and the extent of this deformation is used to estimate their viscosity (Supplementary Note 7). The viscosity estimates shown in Fig. 3b indicate high fractions (40–80%, for the four samples) of solid particles with a viscosity of $\geq 10^{10}$ Pa s, similar to plastic materials[29]. Such high viscosity indicates that they originate either from a partial disintegration of the resin tube material or from aqueous-phase polymerization of the soluble components of the waste as the aerosol mist dries out[29].

Computer-controlled SEM with energy-dispersed X-ray microanalysis (CCSEM–EDX) performed on over >2,000 particles in each of the four samples showed their predominantly carbonaceous composition, with only minor contributions from inorganic salts or mineral dust (Supplementary Note 9), consistent with the suggested designation

https://doi.org/10.1038/s41565-022-01219-9

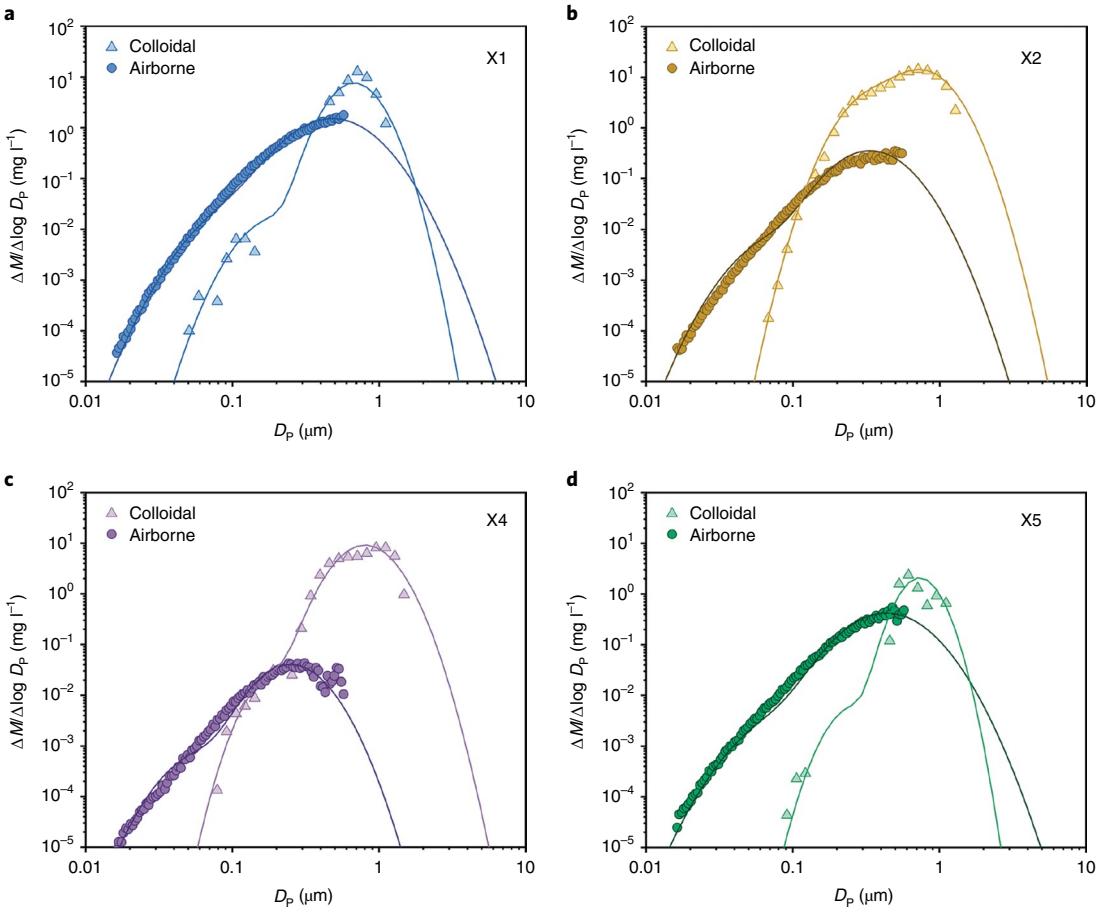

Fig. 2 | Particle mass size distributions of wet colloids and dry particles from CIPP waste. Particle mass size distributions of wet colloids in CIPP waste condensate samples and dry particles aerosolized from the same samples collected at four different operation sites (X1, X2, X4 and X5). The lines show bimodal lognormal data fits; the fitting parameters are tabulated in Supplementary Table 2. D_p, particle diameter; $\Delta M/\Delta\log D_p$, mass concentration. The mass concentration values are reported in units of milligrams of solid material (colloids or particles) per litre of discharged condensate.

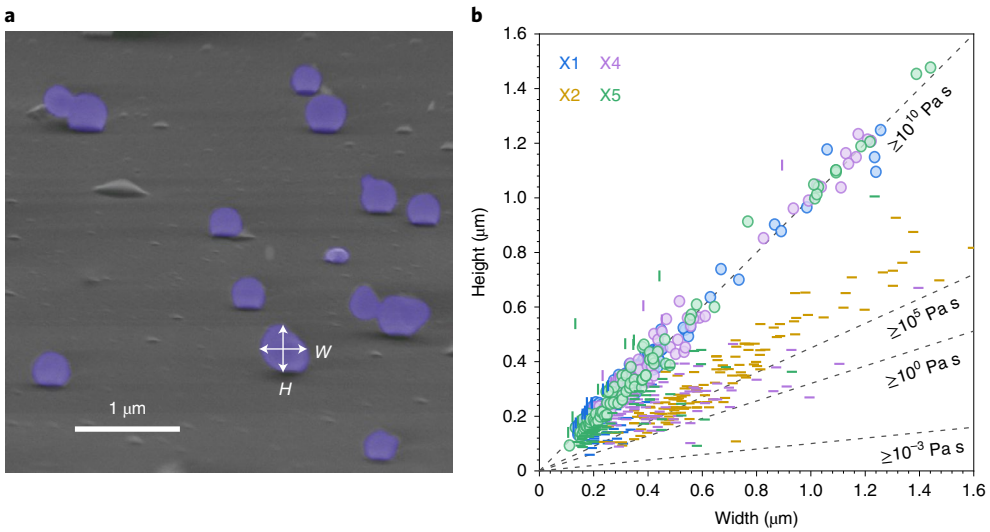

Fig. 3 | Size, morphology and viscosity characteristics of dry particles aerosolized from four samples of CIPP waste condensate. a, SEM image (in secondary electron mode) of particles imaged at a tilt angle of 75°, showing the particle morphology after impact on a substrate. Particles with high viscosity remain spherical after impact; liquid-like particles exhibit a flat morphology. *H*, height; *W*, width. **b**, Plot of particle height versus their width after impact, referenced to particle standards of known viscosity (Supplementary Fig. 5). The viscosity characteristics of individual particles are inferred by comparison with the references (indicated by dashed lines). Circles correspond to spherical particles; vertical and horizontal line markers correspond to high-dome and flat particles, respectively.

https://doi.org/10.1038/s41565-022-01219-9

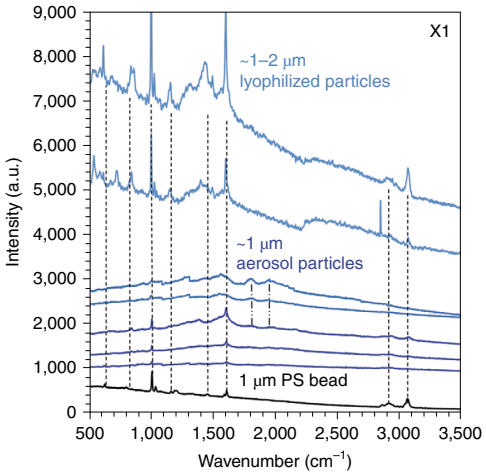

Fig. 4 | SERS spectra of individual dry EnvNP particles from the X1 sample of CIPP waste condensate. Representative SERS spectra of single particles from lyophilized residue (top two spectra) and individual dry airborne particles collected on a substrate. The dashed lines show the similarity between the spectral characteristics of a subset of particles and a standard PS microbead as reference. The apparent PS spectral features[16,17] are as follows: stretching modes of aliphatic C–H at 2,931 cm^{-1} (asym.) and 2,868 cm^{-1} (sym.), stretching of aromatic C–H at 3,075 cm^{-1} and bending at 1,435 and 1,154 cm^{-1}, C=C vibration at 1,602 cm^{-1}, 'breathing mode' of the aromatic ring at 1,000 cm^{-1}, the combination band of the CH out-of-plane bending modes from the ring and the CH_2 rocking modes from the backbone at 852 cm^{-1} and C–C vibration at 614 cm^{-1}. The dashed-dotted lines indicate additional spectral characteristics specific to poly(styrene maleic anhydride)[31], corresponding to C=O stretching at 1,889 and 1,807 cm^{-1}, observed in some of the particles. a.u., arbitrary units.

of these particles as EnvNPs. Furthermore, the vibrational spectra of individual particles recorded by surface-enhanced Raman spectroscopy (SERS) show the spectroscopic features of common microplastic materials (Supplementary Note 8). Figure 4 shows selected SERS spectra of relatively large (>1 μm) dry particles obtained from the waste condensates. These EnvNPs are likely polymers, with characteristic features in the 3,000 cm^{-1} region. In particular, polystyrene (PS) resonances are evident in the spectra of some of the particles, revealed by comparison with a PS microbead standard. Furthermore, particles exhibiting SERS signatures of other polymer materials, such as poly(styrene maleic anhydride) and polydimethylsiloxane, are also noteworthy (Supplementary Fig. 6)[30,31]. The top two SERS spectra in Fig. 4 were recorded for ~2 μm particles from lyophilized waste analyte from the X1 sample. These spectra show features similar to the PS standard. However, because of only minute quantities and the chemical complexity of the analytes in EnvNP particles, the features are relatively broad and have very low intensities, which renders their analysis difficult. Moreover, the detection limit of SERS for organic particles is ~1 μm, which hinders the detection of submicrometre EnvNPs. The spectral data shown in Fig. 4 and Supplementary Fig. 6 demonstrate the need to identify the composition of dry EnvNPs from CIPP emissions at scales finer than those accessible by SERS.

Synchrotron-based scanning transmission X-ray microscopy (STXM) enables the imaging of carbon speciation, allowing differentiation between different polymers distributed within internal particle structures with a lateral resolution of ~35 nm. Particle-specific ratios of the total carbon absorption to the particle diameter derived from STXM measurements were used to distinguish solid spherical EnvNPs from flat, domed particles having lower viscosity (Supplementary Note 10). Figure 5a shows the STXM images of selected solid EnvNP particles and their associated near-edge X-ray absorption fine structure (NEXAFS) spectra acquired at their carbon K-edge energy. The NEXAFS spectra of the EnvNP particles share similar characteristics with reported thin-film polymer standards[32] (Supplementary Note 10), with differences arising due to their multicomponent composition. Because of the chemical complexity of the emissions discharged from CIPP installations, the NEXAFS spectra of the investigated EnvNP samples are best interpreted as a mixture of multiple polymers. The systematic differences between the NEXAFS spectra of the solid particles identified in the aerosolized samples generated from the four waste condensates indicate that the chemical composition of the EnvNPs varies substantially between worksites where different operating conditions are employed. Figure 5b shows the composition maps of individual solid particles generated in our experiments, indicating that their interiors are dominated by organic components. Unlike the typical particles of urban photochemical smog, where the components of secondary organic aerosol tend to coat the inorganic and black carbon inclusions from primary emissions[33], the particles reported here show either organic-only composition or an inverted morphology of organic cores coated with inorganic components. This inverted morphology is consistent with the assumption that organic cores originate from the insoluble organic colloids present in the discharged waste condensate and are coated with thin layers of inorganic salts (probably carbonates) formed by precipitation as the microdroplets of wet aerosol dry out. It is also expected that additional organic solid particles may be formed by the condensation of soluble organic components that have polymerized in drying microdroplets. A quantitative assessment of organic volume fractions (OVFs) in individual particles by X-ray spectromicroscopy (Fig. 5c,d and Supplementary Note 10) showed overall minor contributions of inorganic salts in the observed particles. It is suggested that lateral chemical heterogeneity and the physical states of the atmospheric EnvNP particles from CIPP operations are likely influenced by both the resin material and specific curing conditions. Therefore, documenting the mass loading, composition and size of individual EnvNP particles collected at worksites and in systematic laboratory tests of CIPP emissions will allow source apportionment of this type of particle in real-world urban environments, prediction of their physical properties and evolution upon atmospheric ageing.

The deposits of white powder commonly observed on trees and other surfaces next to CIPP installation sites (Supplementary Note 12) are likely to be micro- and nanoplastic particles emitted during the process[17]. While it may be surprising that EnvNP particles have not been explicitly reported in the assessments of CIPP emissions and in more general studies characterizing the urban aerosol, there are compelling reasons for their lack of observation. EnvNP particles are resistant to decomposition on heating up to 400 °C observed in high-resolution transmission electron microscopy (HRTEM) experiments (Supplementary Note 11), suggesting that in situ particle analysis using thermoanalytical methods is unsuitable for their detection. Thus, if EnvNP particles were present in urban environments, common thermal desorption-based aerosol mass spectrometers would underestimate the organic particle concentration. Laser ablation single-particle mass spectrometry would detect EnvNP particles. However, extensive fragmentation of organic analyte on ablation would make it difficult to distinguish EnvNPs from other organic particles. Due to their solid, spherical morphology and polymer composition, off-line spectromicroscopy methods are likely to be advantageous for the detection and characterization of fine EnvNPs[33].

Public records indicate that 61–454 tonnes of resin are used for each CIPP project in US urban areas, where multiple sewer pipes are typically repaired (Supplementary Note 13)[16]. Laboratory studies show that, during the CIPP process, ~9 wt% of the organic resin material is discharged into the air[16], which translates into >5 tons of organic chemical waste released into atmospheric and aquatic environments as gas- and condensed-phase emissions for each CIPP project[12,14,16,17,34,35]. Based on a conservative estimate that the mass fraction of EnvNP particles is only ~5% of the total organic waste

https://doi.org/10.1038/s41565-022-01219-9

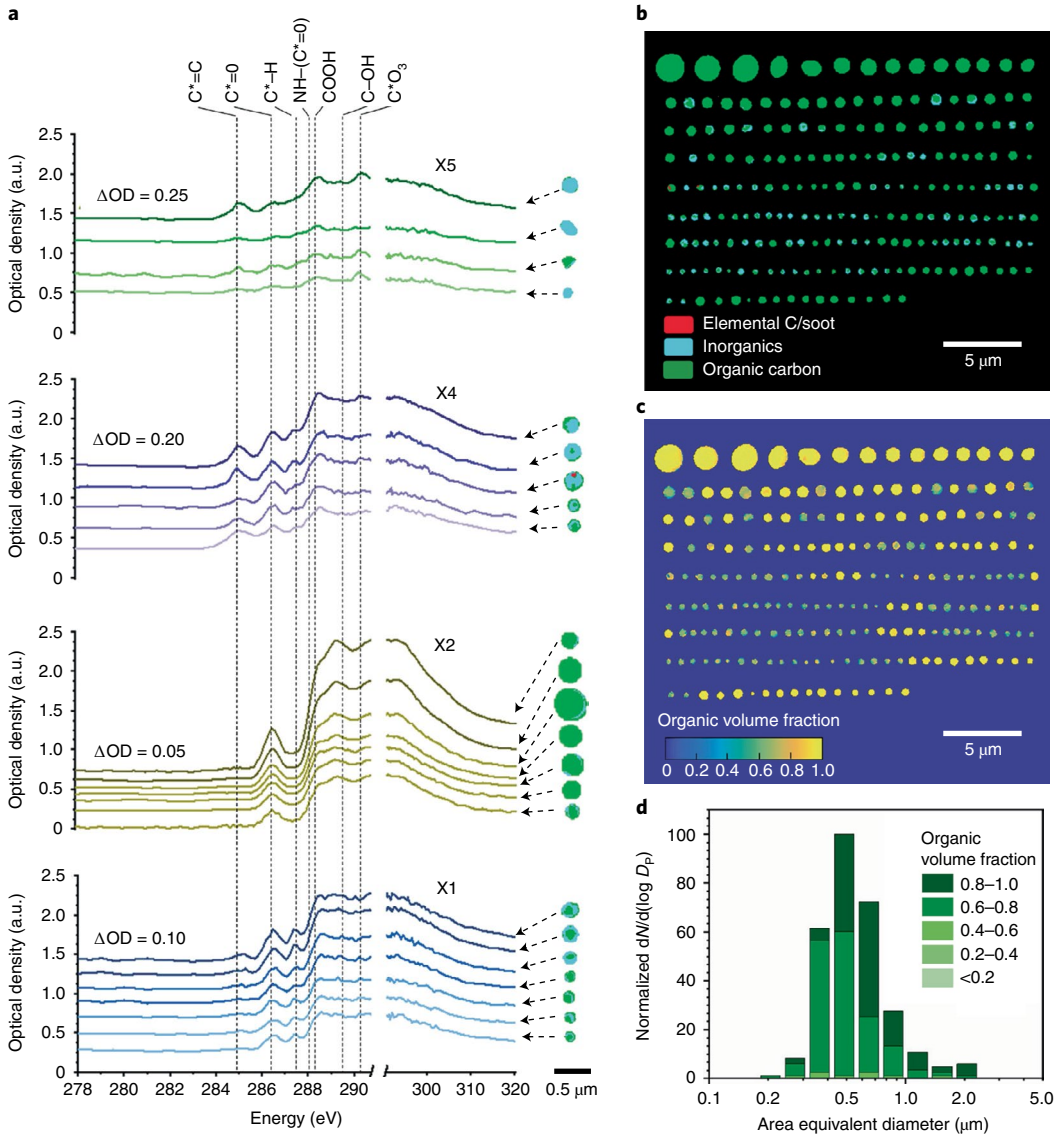

Fig. 5 | Carbon chemical bonding and mixing states of the EnvNPs from CIPP waste condensates. a, Carbon K-edge NEXAFS spectra of representative individual solid EnvNP particles from the four samples X1, X2, X4 and X5 (left). The corresponding individual particle maps show the organic carbon (green), black carbon (red) and inorganic (blue) content, which overlap for some particles (right). For each of the sample groups, the spectra are offset by incremental optical density (ΔOD) values, indicated in the legends. The dashed lines indicate the absorption of various carbon-containing groups. The characteristic peaks of X1 at 286.7 eV (C*=O), 287.7 eV (C*–H) and 288.5 eV (COOH) coincide with the peak positions of poly(acrylonitrile) and poly(vinyl alcohol) materials[18]. The single dominant spectral feature of X2 at 286.7 eV (C*=O) is indicative of poly(vinyl methyl ketone), widely used in industry as a crosslinked film[18]. Samples X4 and X5 show similar NEXAFS features at 284.9 eV (C*=C), 286.7 eV (C*=O), 287.7 eV (C*–H), 288.5 eV (COOH) and 290.4 eV (C^*O_3), which align with poly(α-methylstyrene), polyether ether ketone and polystyrene (Supplementary Note 9). * denotes the 1s → σ* transitions. **b**, STXM composition maps for all samples indicate particles dominated by organic carbon. **c**, OVF maps of the same particles derived from quantitative analysis of the NEXAFS spectra of the particles. **d**, Histogram of the OVF values determined for individual particles plotted as a function of particle size show only minor contributions from inorganic components.

(Supplementary Table 1), their emission will be >0.25 tons per project. This scale of urban pollution is not well documented. In fact, it may eclipse many other common sources of pollution in urban areas. Many recent studies have shown that emissions from CIPP technology pose serious health risks to workers and the nearby public[17,36,37]. Their results have led to US federal[38,39], California and Florida state[40,41], and industry actions, acknowledging the critical need to mitigate CIPP emissions due to human health effects and environmental impacts. However, all studies conducted so far have been limited to gas-phase and water-soluble chemical emissions, while emissions of EnvNP particles have not been considered.

Therefore there is an urgent need to quantitatively characterize the emissions of EnvNPs produced during CIPP manufacture as their environmental discharge and human exposure continue to occur. At present, little is known about which specific manufacturing conditions can be altered to reduce the emissions of EnvNPs and other pollutants. To provide evidence-based practical solutions for safer (less polluting) CIPP operation, systematic studies are needed to investigate how changing the resin, curing temperature, heating time, steam and other ingredient levels may affect the magnitude and composition of CIPP emissions, and to compare these with future field measurements.

Online content

Any methods, additional references, Nature Research reporting summaries, source data, extended data, supplementary information, acknowledgements, peer review information; details of author contributions and competing interests; and statements of data and code availability are available at https://doi.org/10.1038/s41565-022-01219-9.

References

1. Schirinzi, G. F. et al. Cytotoxic effects of commonly used nanomaterials and microplastics on cerebral and epithelial human cells. *Environ. Res.* **159**, 579–587 (2017).
2. Prata, J. C., da Costa, J. P., Lopes, I., Duarte, A. C. & Rocha-Santos, T. Environmental exposure to microplastics: an overview on possible human health effects. *Sci. Total Environ.* **702**, 134455 (2020).
3. Lehner, R., Weder, C., Petri-Fink, A. & Rothen-Rutishauser, B. Emergence of nanoplastic in the environment and possible impact on human health. *Environ. Sci. Technol.* **53**, 1748–1765 (2019).
4. Gigault, J. et al. Nanoplastics are neither microplastics nor engineered nanoparticles. *Nat. Nanotechnol.* **16**, 501–507 (2021).
5. *Cured-In-Place Pipe (CIPP) Market Size, Share, Trend, Forecast, and Competitive Analysis: 2020–2025*. Report No. SRCE108; 1–273 (Stratview Research, 2019).
6. Peng, J., Wang, J. & Cai, L. Current understanding of microplastics in the environment: occurrence, fate, risks, and what we should do. *Integr. Environ. Assess. Manag.* **13**, 476–482 (2017).
7. Bucci, K., Tulio, M. & Rochman, C. M. What is known and unknown about the effects of plastic pollution: a meta-analysis and systematic review. *Ecol. Appl.* https://doi.org/10.1002/eap.2044 (2020).
8. Akdogan, Z. & Guven, B. Microplastics in the environment: a critical review of current understanding and identification of future research needs. *Environ. Pollut.* **254**, 113011 (2019).
9. Wu, P. et al. Environmental occurrences, fate, and impacts of microplastics. *Ecotoxicol. Environ. Saf.* **184**, 109612 (2019).
10. Wlasits, P. J., Stoellner, A., Lattner, G., Maggauer, K. & Winkler, P. M. Size characterization and detection of aerosolized nanoplastics originating from evaporated thermoplastics. *Aerosol Sci. Technol.* **56**, 176–185 (2022).
11. Chen, G., Feng, Q. & Wang, J. Mini-review of microplastics in the atmosphere and their risks to humans. *Sci. Total Environ.* **703**, 135504 (2020).
12. Ra, K. et al. Considerations for emission monitoring and liner analysis of thermally manufactured sewer cured-in-place-pipes (CIPP). *J. Hazard. Mater.* **371**, 540–549 (2019).
13. Noh, Y. et al. Emergency responder and public health considerations for plastic sewer lining chemical waste exposures in indoor environments. *J. Hazard. Mater.* **422**, 126832 (2022).
14. Matthews, E., Matthews, J. & Eklund, S. *NASSCO CIPP Emissions Phase 2: Evaluation of Air Emissions from Polyester Resin CIPP with Steam Cure. Final Report* (NASSCO, 2020).
15. Hong, Z. et al. Characteristics of atmospheric volatile organic compounds (VOCs) at a mountainous forest site and two urban sites in the southeast of China. *Sci. Total Environ.* **657**, 1491–1500 (2019).
16. Teimouri Sendesi, S. M. et al. An emerging mobile air pollution source: outdoor plastic liner manufacturing sites discharge VOCs into urban and rural areas. *Environ. Sci. Process. Impacts* **22**, 1828–1841 (2020).
17. Teimouri Sendesi, S. M. et al. Worksite chemical air emissions and worker exposure during sanitary sewer and stormwater pipe rehabilitation using cured-in-place-pipe (CIPP). *Environ. Sci. Technol. Lett.* **4**, 325–333 (2017).
18. Hinds, W. C. in *Aerosol Technology: Properties, Behavior, and Measurement of Airborne Particles* 46–48 (Wiley, 1999).
19. *Initial list of hazardous air pollutants with modifications* (United States Environmental Protection Agency, 2022). https://www.epa.gov/haps/initial-list-hazardous-air-pollutants-modifications
20. NSCEP. *An Exposure and Risk Assessment for Benzo[a]pyrene and Other Polycyclic Aromatic Hydrocarbons*. Report No. EPA-44074-85-020 (NSCEP, 1982).
21. Foster, P. M., Mylchreest, E., Gaido, K. W. & Sar, M. Effects of phthalate esters on the developing reproductive tract of male rats. *Hum. Reprod. Update* **7**, 231–235 (2001).
22. Lee, A. K. Y. et al. Formation of light absorbing organo-nitrogen species from evaporation of droplets containing glyoxal and ammonium sulfate. *Environ. Sci. Technol.* **47**, 12819–12826 (2013).
23. Ortiz-Montalvo, D. L., Schwier, A. N., Lim, Y. B., McNeill, V. F. & Turpin, B. J. Volatility of methylglyoxal cloud SOA formed through OH radical oxidation and droplet evaporation. *Atmos. Environ.* **130**, 145–152 (2016).
24. Bain, R. M., Pulliam, C. J., Thery, F. & Cooks, R. G. Accelerated chemical reactions and organic synthesis in Leidenfrost droplets. *Angew. Chem. Int. Ed.* **55**, 10478–10482 (2016).
25. Petters, S. S. et al. Volatility change during droplet evaporation of pyruvic acid. *ACS Earth Space Chem.* **4**, 741–749 (2020).
26. Nguyen, T. B. et al. Formation of nitrogen-and sulfur-containing light-absorbing compounds accelerated by evaporation of water from secondary organic aerosols. *J. Geophys. Res.: Atmos.* **117**, D01207 (2012).
27. Marsh, B. M., Iyer, K. & Cooks, R. G. Reaction acceleration in electrospray droplets: size, distance, and surfactant effects. *J. Am. Soc. Mass. Spectrom.* **30**, 2022–2030 (2019).
28. Laskin, J. et al. Molecular selectivity of brown carbon chromophores. *Environ. Sci. Technol.* **48**, 12047–12055 (2014).
29. Reid, J. P. et al. The viscosity of atmospherically relevant organic particles. *Nat. Commun.* **9**, 956 (2018).
30. Zhou, X.-X., Liu, R., Hao, L.-T. & Liu, J.-F. Identification of polystyrene nanoplastics using surface enhanced Raman spectroscopy. *Talanta* **221**, 121552 (2021).
31. Schoukens, G., Martins, J. & Samyn, P. Insights in the molecular structure of low- and high-molecular weight poly(styrene-maleic anhydride) from vibrational and resonance spectroscopy. *Polymer* **54**, 349–362 (2013).
32. Dhez, O., Ade, H. & Urquhart, S. G. Calibrated NEXAFS spectra of some common polymers. *J. Electron Spectrosc. Relat. Phenom.* **128**, 85–96 (2003).
33. Laskin, A., Moffet, R. C. & Gilles, M. K. Chemical imaging of atmospheric particles. *Acc. Chem. Res.* **52**, 3419–3431 (2019).
34. Najafi, M. et al. *Evaluation of Potential Release of Organic Chemicals in the Steam Exhaust and Other Release Points During Pipe Rehabilitation Using the Trenchless Cured-In-Place Pipe (CIPP) Method* (NASSCO, 2018).
35. Nuruddin, M. et al. Evaluation of the physical, chemical, mechanical, and thermal properties of steam-cured PET/polyester cured-in-place pipe. *J. Compos. Mater.* **53**, 2687–2699 (2019).
36. Ra, K. et al. Critical review: surface water and stormwater quality impacts of cured-in-place pipe repairs. *J. Am. Water Works Assoc.* **110**, 15–32 (2018).
37. Li, X. et al. Outdoor manufacture of UV-cured plastic linings for storm water culvert repair: chemical emissions and residual. *Environ. Pollut.* **245**, 1031–1040 (2019).
38. US Occupational Safety and Health Administration *Citation and Notification of Penalty, Inspection Number 1274028*. Report No. 0524200 (US Department of Labor, 2017).
39. LeBouf, R. F. & Burns, D. A. *Health Hazard Evaluation Report: Evaluation of Exposures to Styrene During Ultraviolet Cured-in-Place-Pipe Installation*. Report No. 2018-0009–3334 (US

National Institute of Occupational Safety and Health, Centers for Disease Control and Prevention, 2019).
40. *Cure-in-Place Pipe (CIPP): Additional Considerations for Municipalities* (California Department of Public Health, 2017).
41. *CIPP Safety Alert* (California Department of Public Health, 2018).

Methods

Samples of CIPP waste condensates

Aqueous condensates of the exhaust emissions discharged during four CIPP installations in Sacramento, California were collected[17]. One CIPP was manufactured with a non-styrene, low-volatile organic resin, and three were manufactured with a styrene-based resin. Stainless-steel air-sampling manifolds were used at each site to capture and condense airborne emissions, collected in Pyrex bottles as detailed by Sendesi et al.[17]. The samples obtained were sealed and refrigerated at −20 °C pending analysis. In this work the waste samples were aerosolized to evaluate the size distributions and mass loadings of plausible atmospheric particle emissions. The particles obtained were also analysed using chemical imaging techniques. Further analyses were conducted to determine the size distributions and mass loadings of the colloids present in the original bulk samples, and to characterize the major solvent-soluble organic components present in the bulk condensates and to estimate their volatility. Further details are included in Supplementary Notes 1 and 2.

Particle size distributions of colloids and particles

The colloidal material in the waste condensate samples was quantified by dynamic light scattering measurements using a Zetasizer Nano-S instrument (Malvern Panalytical). For quantitative data analysis, the dispersant was assumed to be water, and the optical properties and density of the colloidal material were assumed to be those of polystyrene. The difference between the total organic carbon and the dissolved organic carbon in the waste condensate samples was used to estimate the lower limit of mass loadings of the colloidal material. The particle size distributions of dry aerosolized particles were measured using a scanning mobility particle sizer interfaced with a condensation particle counter (TSI, models 3081 and 3776). The volumes of the condensate samples consumed in the aerosolization experiments were recorded and used to relate the measured mass concentrations and particle size distributions of airborne dry particles to the volume of the waste condensate. The quantitative measurements of colloids and dry airborne particles are presented here as milligrams of colloids (or dry airborne particles) per litre of waste condensate. Additional details of these experiments are included in Supplementary Notes 2–4.

Molecular characterization of waste condensates

The components of the waste condensates extracted in acetonitrile–dichloromethane–hexane (2:2:1, by volume) were separated by reversed-phase high-performance liquid chromatography (HPLC). The separated fractions were characterized by a photodiode array detector (PDA) and a high-resolution mass spectrometer (HRMS) interfaced with electrospray ionization and atmospheric pressure photochemical ionization sources to identify both polar and non-polar organic components[42]. Details of the HPLC–PDA–HRMS analysis are included in Supplementary Note 5.

Chemical imaging of particles

The dry particles from the aerosolization experiments deposited onto solid substrates were imaged by microscopies that revealed both the morphology and spectroscopically determined chemical composition. A SEM microscope was used to image particle samples at a tilt angle of 75° to distinguish between solid (spherical) and liquid-like (flattened) particles. Their viscosities were then inferred from the observed particle height-to-width ratios by comparison with standards of known viscosity. The size and elemental composition of large ensembles of >2,000 particles per sample were analysed by CCSEM–EDX, providing statistically significant data on the particle-type populations and their elemental compositions[43]. Additional details of viscosity measurements by SEM and CCESM-EDX particle analysis are included in Supplementary Notes 7 and 9.

The vibrational spectra of individual solid organic particles were recorded using SERS. At present, Raman spectral features are commonly used to identify environmental microplastic particles and apportion them to the most common polymer types[44]. SERS was used for rapid screening of dry samples to identify the polymer characteristics of EnvNP particles. Specific details of the SERS analysis are included in Supplementary Note 8.

STXM–NEXAFS spectromicroscopy at the carbon K-edge energy was used to obtain information on the chemical bonding of carbon within individual particles at a lateral resolution of ~35 nm, sufficient for a detailed analysis[45] of submicrometre EnvNP particles. Particle component maps[46] were constructed on the basis of NEXAFS spectral features indicative of carbon-specific functional groups and chemical bonding. Combined, the CCSEM–EDX and STXM–NEXAFS datasets allowed the grouping and assessment of EnvNP particle types and their representative mixing states. Additional details of the STXM–NEXAFS analysis are included in Supplementary Note 10.

Data availability

The datasets generated and analysed in this work are available for download as a zip file from https://doi.org/10.4231/XR71-ZM27. Datasets are provided for Figs. 2–5 and Supplementary Figs. 3, 5 and 7–10. Supplementary information is available in the online version of the paper. Correspondence and requests for materials should be addressed to A.L.

References

42. Lin, P., Fleming, L. T., Nizkorodov, S. A., Laskin, J. & Laskin, A. Comprehensive molecular characterization of atmospheric brown carbon by high resolution mass spectrometry with electrospray and atmospheric pressure photoionization. *Anal. Chem.* **90**, 12493–12502 (2018).
43. Laskin, A., Cowin, J. P. & Iedema, M. J. Analysis of individual environmental particles using modern methods of electron microscopy and X-ray microanalysis. *J. Electron Spectrosc. Relat. Phenom.* **150**, 260–274 (2006).
44. Anger, P. M. et al. Raman microspectroscopy as a tool for microplastic particle analysis. *Trends Anal. Chem.* **109**, 214–226 (2018).
45. Moffet, R. C., Tivanski, A. V. & Gilles, M. K. in *Fundamentals and Applications in Aerosol Spectroscopy* (eds Signorell, R. & Reid, J. P.) Ch. 17 (Taylor and Francis, 2010).
46. Moffet, R. C., Henn, T., Laskin, A. & Gilles, M. K. Automated chemical analysis of internally mixed aerosol particles using X-ray spectromicroscopy at the carbon K-edge. *Anal. Chem.* **82**, 7906–7914 (2010).

Acknowledgements

This work was supported by the US National Science Foundation (grant nos. CBET-1624183 and CBET-2129166 (A.J.W. group), and CBET-2107946 (A.L. group)), the National Science Foundation Graduate Research Fellowship Program (grant no. DGE-1333468 (A.C.M.)) and the Purdue University Ross Fellowship program (B.N.P., S.A.L.S. and Y.N.). Any opinions, findings and conclusions or recommendations expressed in this material are those of the author(s) and do not necessarily reflect the views of the National Science Foundation. The CCSEM–EDX, HRTEM and SERS analyses, with guidance from N. Lata and Z. Cheng, were performed at the Environmental Molecular Sciences Laboratory, a National Scientific User Facility sponsored by OBER at PNNL. PNNL is operated by the US Department of Energy by the Battelle Memorial Institute under contract DE-AC06-76RL0. STXM–NEXAFS analyses were performed at beamline 5.3.2 of the Advanced Light Source at Lawrence Berkeley National Laboratory (LBNL), with guidance from D. Kilcoyne, M. Marcus and D. Shapiro. LBNL is supported by the Director, Office

of Science, Office of Basic Energy Sciences of the US Department of Energy under contract DE-AC02-05CH11231. STXM maps of particles were also acquired at the Canadian Light Source (CLS), with guidance from J. Wang. CLS is supported by the Canada Foundation for Innovation, Natural Sciences and Engineering Research Council of Canada, the University of Saskatchewan, the Government of Saskatchewan, Western Economic Diversification Canada, the National Research Council Canada and the Canadian Institutes of Health Research.

Author contributions

A.C.M., J.M.T. and A.L. conceptualized the framework, experiments and analytical methodologies of the study. Y.N., S.M.T.S., B.E.B., J.A.H. and A.J.W. conducted field studies and provided samples of the CIPP waste condensates. A.C.M., C.P.W. and B.N.P. performed the HPLC–HRMS measurements and analysed the data. J.M.T. and F.A.R.-A. analysed individual particles using SEM and STXM. S.A.L.S. performed the TEM analysis of heated particles. S.C. assisted with SEM experiments and R.C.M. assisted with STXM experiments and instrument operation. B.T.O'C. and P.Z.E.-K. performed the SERS analysis. A.C.M. and A.L. integrated the experimental datasets and wrote the manuscript, and all authors contributed its review and editing. A.J.W. and A.L. secured grant support for this study and managed the project.

Competing interests

A.J.W., J.A.H., B.E.B. and S.M.T.S. are named in a patent application (PCT application no. PCT/US18/28173) filed 18 April 2018 by the Purdue Research Foundation. The patent application pertains to the technologies for capturing CIPP waste condensates investigated in this study. The invention was developed with support from the US National Science Foundation (grant CBET-1624183). The remaining authors declare no competing interests.

Additional information

Supplementary information The online version contains supplementary material available at https://doi.org/10.1038/s41565-022-01219-9.

Correspondence and requests for materials should be addressed to Alexander Laskin.

Peer review information *Nature Nanotechnology* thanks the anonymous reviewers for their contribution to the peer review of this work.

nature nanotechnology

Letter

https://doi.org/10.1038/s41565-022-01219-9

Atmospheric emission of nanoplastics from sewer pipe repairs

In the format provided by the authors and unedited

SUPPLEMENTAL MATERIAL FOR

Atmospheric emission of nanoplastics from sewer pipes repair

Ana C. Morales,[1] Jay M. Tomlin,[1] Christopher P. West,[1] Felipe A. Rivera-Adorno,[1] Brianna N. Peterson,[1] Steven A. L. Sharpe,[1] Yoorae Noh,[2] Seyedeh M. T. Sendesi,[2] Brandon E. Boor,[2] John A. Howarter,[3] Ryan C. Moffet,[4] Swarup China,[5] Brian T. O'Callahan, [6] Patrick Z. El-Khoury,[5] Andrew J. Whelton,[2,7] Alexander Laskin[1,*]

[1]*Department of Chemistry, Purdue University, West Lafayette, IN, USA*

[2]*Lyles School of Civil Engineering, Purdue University, West Lafayette, IN, USA*

[3]*School of Materials Engineering, Purdue University, West Lafayette, IN USA*

[4]*Sonoma Technology, Inc., Petaluma, CA, USA*

[5]*Physical Sciences Division, Pacific Northwest National Laboratory,* [6]*Environmental Molecular Sciences Laboratory, P.O. Box 999, Richland, Washington 99352, USA*

[7]*Department of Environmental and Ecological Engineering, Purdue University, West Lafayette, IN, USA*

*Correspondence to *alaskin@purdue.edu*

Table of Contents

Supplementary Note 1: Collection, Storage, and Use of the CIPP Discharged Steam Condensates.

In August 2016, samples of discharged waste from CIPP installations were collected at outdoor locations in Sacramento, California as described in detail by Sendesi et al. (2017).[1] At each sampling site, stainless steel air manifolds were set up at an exhaust point to capture and condense materials from the air. At the exhaust point, the air stream was condensed by ambient cooling and passage of the air stream through ice chest condensers and collected in Pyrex bottles.[1] All condensates were stored at –20 ºC to prevent subsequent reactions after collection.

Sendesi et al. (2017)[1] reported the chemical composition and toxicological significance of selected emitted materials identified by gas chromatography - mass spectrometry (GC-MS) and nuclear magnetic resonance (NMR) spectroscopy. Ra et al. (2019) further described air testing results from this site.[2] The discharged waste emissions were determined to be a multi-phase chemical mixture of organic vapor, particulates, and liquid droplets, where particulates were hypothesized to be a mixture of condensable vapor and partially cured resin. This complex mixture was confirmed to contain hazardous air pollutants, known and suspected carcinogens, endocrine disrupting compounds, and uncured resin material.[1] However, the composition of particulates was not investigated.

Two types of resin were employed during CIPP operation at the investigated sites: a styrene-based resin and a low-volatility organic compound (VOC) non-styrene resin. Vipel® isophthalic based polyester resin was used for the styrene based CIPP installations (sites X1, X4, and X5) with 0.5% Trigonox® KSM and 1% di-(4-*tert*-butylcyclohexyl) peroxy dicarbonate initiators and contained 32.0% wt. of styrene.[1] The low-VOC, non-styrene based installation (site X2) used EcoTek™ L040-TNVG-33 vinyl ester resin with 30% - 35% wt. dioxotetraoxatrimethylalkadiene, but the initiators were not disclosed.[1,3]

Styrene concentration in condensates was characterized by GC-MS-TQ8040 (Shimadzu Co.). Quantification of samples was performed using 1 ppm of 1,4-dichlorobenzene-d4 (Supelco Inc.) as an internal standard. The total organic carbon (TOC) concentration was measured using a TNM-L ROHS (Shimadzu Co.) analyzer in accordance with USEPA method 415.1.[4] The instrument was calibrated from 0 to 200 mg TOC per liter of sample using potassium hydrogen phthalate (R^2=0.99). In order to measure the dissolved organic carbon level, the samples were filtrated by a 0.5 μm glass fiber filter (Fisher Scientific) and measured with the same method for

70 TOC. Styrene concentrations, total organic carbon, and dissolved organic carbon values are presented in Table S1.

Table S1. Summary of CIPP condensates used in this study and the corresponding styrene concentrations, total organic carbon, and dissolved organic carbon values. Aerosol mass
75 concentrations were determined by measurements in this study, discussed in Supplementary Note 3. All mass concentrations are reported here in the units of milligram of solid material (colloids or particles) per liter of the discharged condensate.

	X1	**X2**	**X4**	**X5**
	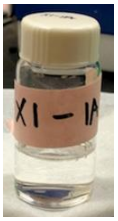	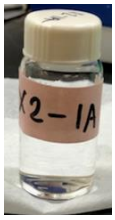	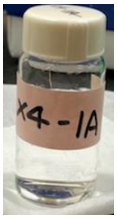	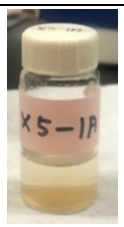
Styrene resin (Y/N)	Yes	No	Yes	Yes
Styrene Resin Concentration (ppm)	4329 ± 937	7.495 ± 0.6	1819 ± 504	2083 ± 35
Total Organic Carbon (mg/L)	33.85	133.4	53.76	13.18
Dissolved Organic Carbon (mg/L)	30.96	127.2	50.47	12.71
Aerosol Mass Concentration Lower Limit (mg/L)	1.65	0.93	0.01	0.19
Aerosol Mass Concentration Upper Limit (mg/L)	3.24	1.01	0.04	0.34

Supplementary Note 2: Overview of the Chemical Analysis Methods.

The multi-phase chemical mixtures initially reported in Sendesi et al. (2017) were investigated using NMR and GC-MS,[1] however the individual particle physicochemical properties found in these mixtures were not investigated. We employ a range of instrumentation in this study to determine the concentration of colloidal materials present in the CIPP discharged waste condensates and to investigate the chemical composition of their resulting dry residues. The combination of several techniques provides molecular-level analysis of the condensate mixtures, single-particle investigations of compositional variability, and estimations of emission rates of EnvNP (Figure S1).

Quantitative in-situ measurements of the colloidal particle size distributions were conducted using dynamic light scattering (DLS) (Supplementary Note 3). Number concentrations and size distributions of the dry, aerosolized particles were determined using a scanning mobility particle sizer (SMPS). Estimations of the EnvNP emissions for each site were determined using the DLS and SMPS measurements and reported in units of milligram of solid material (colloids or particles) per liter of the discharged condensate (Supplementary Notes 3 and 4).

Molecular-level analysis of the bulk CIPP waste condensates provides a quantitative assessment of the chemical composition and physical properties of emitted materials. Bulk analysis of the condensable materials was conducted using high-performance liquid chromatography (HPLC) equipped with a photodiode array (PDA) and high-resolution mass spectrometry (HRMS) (Supplementary Note 5). Solvent-soluble species were extracted in a mixture of organic solvents (acetonitrile/dichloromethane/hexane = 2:2:1 by volume) and separated using reversed-phase HPLC. Resin components and other hazardous materials were identified, and their corresponding volatilities were estimated. Molecular characteristics of the bulk residues were also investigated using surface enhanced Raman spectroscopy (SERS) after lyophilization of the condensates (Supplementary Note 7). SERS is a common technique used to identify micro- and nanoplastic materials in environmental (marine and terrestrial) samples, therefore all spectra obtained were compared to known plastic reference spectra.[5]

Single-particle analysis of dried aerosol particles was achieved by nebulizing the condensates using nitrogen and drying the particles in drying tubes filled with calcium sulfate desiccant. Dried particles were collected in a micro-orifice uniform deposit impactor (MOUDI).

Particles collected on stage 6 (0.56-1.00 µm), stage 7 (0.32-0.56 µm) and stage 8 (0.18-0.32 µm) were investigated using several spectro-microscopic techniques.

Individual particles (>1 µm) were investigated using SERS and compared to plastic reference spectra. SERS measurements did not provide a fine enough lateral resolution necessary for investigating EnvNP (particles <1 µm). This limit is inherent to the diffraction-limited optical measurement. Moreover, smaller EnvNP particles in the sub-micron range develop plasmon resonances that lead to backgrounds associated with Raman scattering and photoluminescence from hot electrons.[6] This obscures the spectroscopic detection of EnvNP. Therefore, computer-controlled scanning electron microscopy with energy dispersed X-ray microanalysis (CCSEM-EDX) and synchrotron-based scanning transmission X-ray microscopy (STXM) were also employed. CCSEM-EDX was employed to analyze the size, elemental composition, and viscosity of individual particles (Supplementary Notes 6 and 8). STXM complemented by Near Edge X-ray Absorption Fine Structure (NEXAFS) spectro-microscopy at the carbon K-edge energy was used to acquire quantitative information regarding chemical bonding and internal mixing of individual particles with a lateral resolution of ~20 nm (Supplementary Note 9).

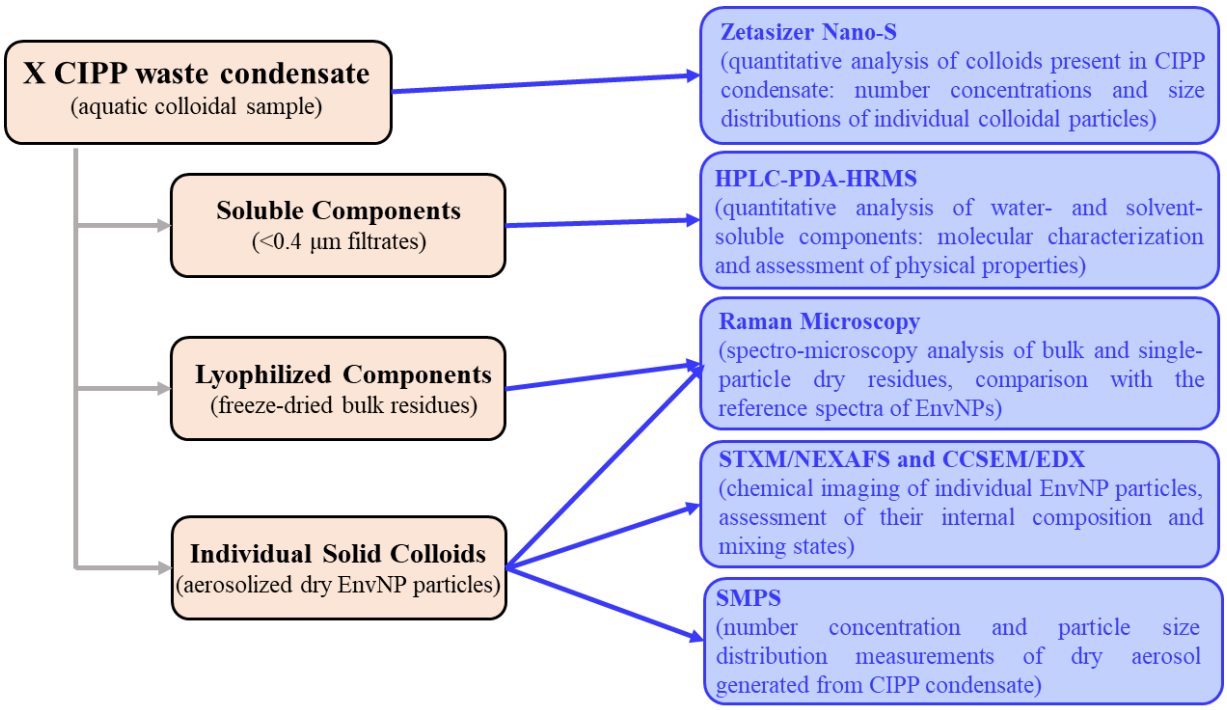

Figure S1. Diagram representing experimental methods employed for analysis of the discharged waste condensates.

Supplementary Note 3: Dynamic Light Scattering Measurements of Colloids.

Colloidal components of the CIPP condensates were analyzed using DLS to investigate the particle number concentration and size distributions in situ. DLS experiments were performed using Zetasizer Nano-S (Malvern Panalytical). A volume of 1.5 mL was transferred from sample stock solutions to a quartz cuvette for measurements. The dispersant was assumed to be water and the material was assumed to be polystyrene (PS). The backscattering angle was 173° by default; water viscosity was set to 8.9×10^{-2} Pa·s; the equilibrium temperature was 25 °C; the refractive index of the PS material was set to $RI = 1.590+i\cdot0.010$. DLS detects number of photons attenuated by colloids and reports measurements in the units of kilo counts per second (kcps), recorded in individual particle size bins (16 per decade). To acquire data over all 16 size bins, each measurement had a 30 second waiting time, and six measurements were taken for each DLS experiment to record I_i values. Obtained data was used to calculate the mass-based particle size distributions (PSD) of colloidal particles assuming that I_i values are proportional to the number of particles (ΔN_i) detected within size bin i.

$$\Delta N_i = Const \times I_i \tag{E1}$$

Then, mass PSD values corresponding to each of the bins i were calculated as

$$\frac{\Delta M_i}{\Delta \log D_p} = \frac{\rho \frac{\pi}{6} \mathrm{D_{p,i}}^3 \Delta N_i}{\log D_{p,i} - \log D_{p,i-1}} = \frac{\rho \frac{\pi}{6} \mathrm{D_{p,i}}^3 \times Const \times I_i}{1/16} \tag{E2}$$

where particle density (ρ) was assumed 1 gr/cm^3 and value of *Const* was set to stipulate assumption of

$$\sum_{i=1}^{16} \Delta M_i = [TOC] - [DOC] \tag{E3}$$

where [*TOC*] and [*DOC*] are mass concentrations (mg/L) of total and dissolved organic carbon, respectively; measured for each of the waste condensates (Table S1)

Supplementary Note 4: Size Distribution Measurements and Mass Loadings of Aerosolized Particles

To investigate the ability of colloids to become airborne particles, the CIPP condensates were nebulized to generate wet aerosol, which was conditioned in drying tubes and the resulting dry residuals were analyzed. A schematic of the experimental setup is shown in Figure S2. Condensates were aerosolized by loading 5 mL in a medical nebulizer cup and blowing 2.1 L min^{-1} of dry nitrogen (N_2) through the cup. The stream of aerosolized mist was then directed through two drying tubes loaded with calcium sulfate desiccant that resulted in relative humidity (RH) of 18% at the exit from the second tube. Particle number concentrations (N_i, i is an individual size bin) of dry aerosol were measured using a scanning mobility particle sizer (SMPS) containing a differential mobility analyzer (TSI model no. 3081) interfaced with a condensation particle counter (CPC, TSI model no. 3776). The SMPS-CPC was operated in low flow mode (sheath and aerosol flows are 3.1 L min^{-1} and 0.31 L min^{-1}, respectively) at particle size resolution settings of 64 bins per decade. Prior to the measurement, the stream of dry aerosol was split between the SMPS-CPC and inlet and, an exhaust line to remove excess flow.

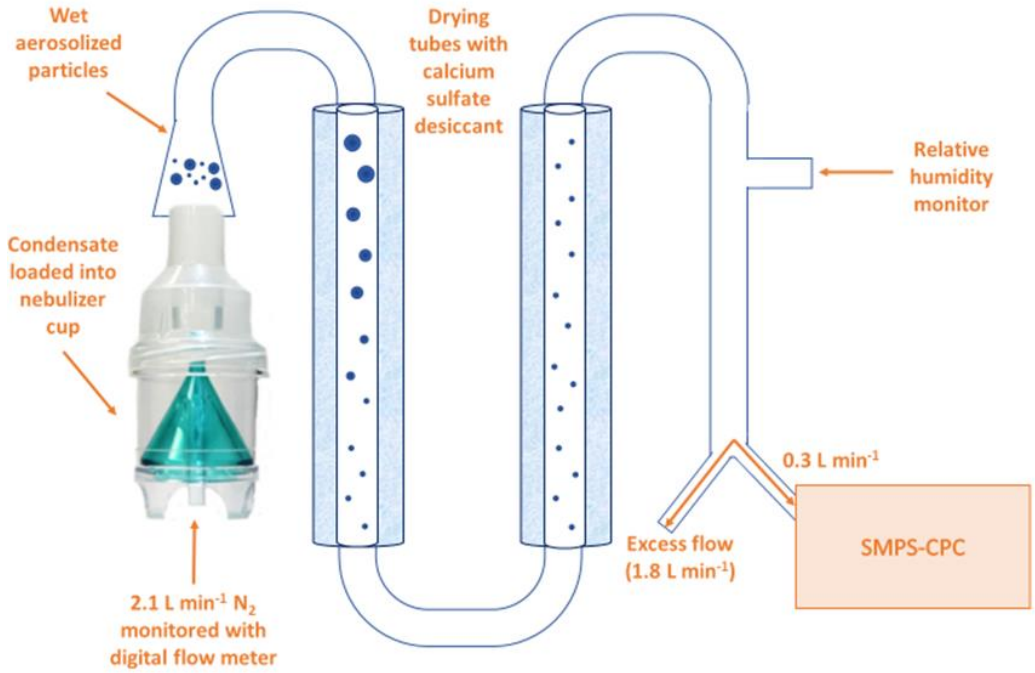

Figure S2. Diagram representing the condensate nebulizing experiment, during flow diagram and detection/counting of dry aerosolized particles.

The SMPS-CPC detects number of particles (ΔN_i) detected in individual size bins i (64 per decade). Airborne number concentrations were converted to mass PSD values using the following equation (assuming ρ=1.05 g/cm^3 – density of polystyrene)

$$\frac{\Delta M_{air,\ i}}{\Delta \log D_{p,i}} = \frac{\rho \frac{\pi}{6} \mathrm{D_{p,i}}^3 \Delta N_i}{\log D_{p,i} - \log D_{p,i-1}} = \frac{\frac{\pi}{6} \mathrm{D_{p,i}}^3 \Delta N_i}{1/64} \quad \text{(E4)}$$

Mass PSD values of $\Delta M_{air,\ i}/\Delta log D_{p,i}$ (mg per L of air) were then scaled to obtained mass PSD values of $\Delta M_i/\Delta log D_{p,i}$ (mg per L of waste condensate) using the conversion equation of

$$\frac{\Delta M_i}{\Delta \log D_{p,i}} = \left(\frac{Q \times t}{V}\right) \times \frac{\Delta M_{air,\ i}}{\Delta \log D_{p,i}} \quad \text{(E5)}$$

where Q is the N_2 flow rate through the cup (2.1 L min^{-1}), t (min) is the duration of experiment, V (L) is the volume of condensate nebulized during the experiment.

Experimental data of $\Delta M_i/\Delta log D_{p,i}$ versus $D_{p,i}$ obtained for colloidal (DLS measurement) and airborne (SMPS measurement) particles were fit with bimodal lognormal PSD functions using equations E6 and E7 for each of the modes.

$$\frac{dM}{d\ log\ D} = \frac{M_T}{\sqrt{2\pi} log\ \sigma_g} exp\left[-\frac{\left(log\ D - log \bar{D}_{gM}{}^2\right)}{2\left(log\ \sigma_g\right)^2}\right] \quad \text{(E6)}$$

$$\sigma_g = \sqrt{\frac{\sum_{i=1}^{N_{bins}} (y_{meas} - y_{fit})^2}{N_{bins} - 1}} \quad \text{(E7)}$$

where M_T is the total mass of particles, σ_g is the standard deviation, D is the particle diameter, and $\bar{D}_{g,M}$ is the geometric mean particle diameter. Table S2 summarizes all fitting parameters of the PSD data.

Table S2. Fitting parameters used for bimodal DLS and SMPS mass size distributions presented in Figure 2 of the manuscript.

	SMPS						DLS					
	$M_{T,1}$ (mg/L)	$D_{g,1}$ (nm)	σ_1	$M_{T,2}$ (mg/L)	$D_{g,2}$ (nm)	σ_2	$M_{T,1}$ (mg/L)	$D_{g,1}$ (nm)	σ_2	$M_{T,2}$ (mg/L)	$D_{gg,2}$ (nm)	σ_3
X1	1.58	55	1.50	66.7	210	1.45	0.01	120	1.35	5.00	500	1.25
X2	0.29	40	1.45	12.3	170	1.40	1.80	240	1.30	9.50	500	1.30
X4	0.03	35	1.40	1.19	145	1.35	0.12	150	1.25	0.22	530	1.30
X5	0.18	40	1.50	17.7	190	1.45	1.00	200	1.25	1.00	600	1.20

Quantitative assessment of the mass loadings of the condensed-phase organic material emitted as dry airborne particles per liter of condensate was determined using the SMPS-CPC data. The lower limit was determined assuming particle size range limited to SMPS experimental observations (i.e., PSD was integrated over 15-650 nm size range):

$$\text{Lower limit: } min\, M_T = \int_{15\ nm}^{650\ nm} M(D_p) dD_p \quad \text{(E8)}$$

The upper limit was then estimated by integrating the lognormal fit of the data over entire size range of particles:

$$\text{Upper limit: } \max M_T = \int_0^{\infty} M(D_p) dD_p \quad \text{(E9)}$$

Notably, the size distributions of the dried aerosolized particles (Figure 2) show that they are well below <1 μm – the respirable size that can successfully penetrate the lungs and potentially enter the blood stream. Mass distributions of both colloids *in situ* and dried residuals (Figure 2 of the manuscript) revealed a substantial concentration of solid materials plausibly released at CIPP installation sites, between 0.01 and 3.24 mg L^{-1} among the four reported samples.

Supplementary Note 5: HPLC-PDA-HRMS Separation and Analysis of the Bulk Samples

Molecular characterization of the CIPP condensates was conducted to investigate chemical composition their components. CIPP waste condensates were extracted using a mixture of organic solvents (acetonitrile/dichloromethane/hexane = 2:2:1 by volume; Optima LC/MS grade, Fisher Chemical) with broad polarity to extract. This organic mixture was selected based on literature reports indicating high extraction efficiency for functionalized organic compounds, ideal for EnvNP.[7,8] The extraction mixture was vortexed for 30 seconds in triplicate at 3000 rpm to facilitate dissolution of organic analyte. The extracts were then filtered using syringe filters with 0.20 μm PTFE membrane to remove insoluble residues. Filtered extracts were dried down to 100 μL using a Turbo Vap nitrogen blowdown vortex evaporation system (Biotage) and reconstituted in 100 μL of acetonitrile. Visible precipitates formed during the preconcentration procedure, so all samples were filtered again using syringe filters with 0.20 μm PTFE membrane to remove insoluble precipitates.

Obtained extracts were analyzed using a high-performance liquid chromatography (HPLC) system (Vanquish) coupled with a photodiode array (PDA) detector and a high-resolution Orbitrap mass spectrometer (HRMS) Q Exactive HF-X (all from Thermo Scientific Inc). The chromatographic separation and HRMS detection of carbon-containing analytes was achieved using a reversed-phase column (Luna C18(2), 150 × 2 mm, 5 μm particles, 100 Å pores; Phenomenex Inc.) following an adapted version of separation protocol described in Lin et al. (2018) and Hettiyadura et al. (2021).[8–10] HRMS detection of the LC-eluted analytes was performed using electrospray ionization (ESI) and dopant-assisted atmospheric pressure photoionization (APPI) sources operating in positive and negative modes, covering a broad range of the analyte components with different polarities.[8,10] A mixture of 3-trifluoromethylanisole (TFMA; 98% purity, Alfa-Aesar) and chlorobenzene (1:99, v/v; anhydrous, 99.8% purity, Sigma-Aldrich) was used as the dopant. Before entering the ionization source, the dopant was delivered to the LC outflow stream at a flow rate of 20 μL min^{-1} using a syringe pump (Thermos Inc.). It was found that the formic acid in the HPLC mobile phase contributed to substantial ion suppression in the APPI negative mode, therefore it has been omitted from this study. Details on the HPLC-PDA-HRMS data acquisition and analysis can be found in Hettiyadura et al. (2021).[10]

The volatility of identified individual compounds are calculated using parameterization from *Li et al.* (2016)[11]:

$$log\ C_0 = (n_C^0 - n_C)b_C - n_O b_O - 2\frac{n_C n_O}{n_C + n_O} b_{CO} - n_N b_N - n_S b_S \quad \text{(E10)}$$

where C_0 is in the units of μg m^{-3}; n_C, n_O, n_N and n_S are numbers of carbon, oxygen, nitrogen and sulfur atoms in the molecule; the values of n_C^0 and b coefficients are those tabulated in Li et al. (2016)[11] (Table 1) for CH, CHO, CHN, CHON, CHOS, and CHONS groups of species, respectively.

Molecular analysis of the dissolved condensate components showed a very complex mixture of chemical pollutants that can partition between gas-, aqueous-, and solid-phases when water evaporates from the discharged steam. Figure S3 illustrates representative results of the chemical characterization of the X1 extract using a HPLC-PDA-HRMS. A wide range of species with broad variability in molecular weight, molecular structures, and oxidation extent were detected. Molecular structures in Figure S3a and Table S3 show those relevant to the CIPP resin composition (marked by green numbers) and PAH byproducts (marked by blue numbers) unambiguously identified in our analysis. Many of these compounds are likely hazardous air pollutants, known and suspected carcinogens, endocrine disrupting compounds, and compounds with little toxicity data, similar to what was found for the gas phase emissions.[1] The background colors of panel C indicate the volatility basis set (VBS)[12] ranges of organic compounds: volatile (VOC), intermediate volatility (IVOC), semi volatile (SVOC), low volatility (LVOC, light red) and extremely low volatility (ELVOC). SVOC and LVOC properties are estimated for majority of the chemical components present in CIPP condensate, which will create solid EnvNP upon dissipation (drying) of the CIPP discharged waste.

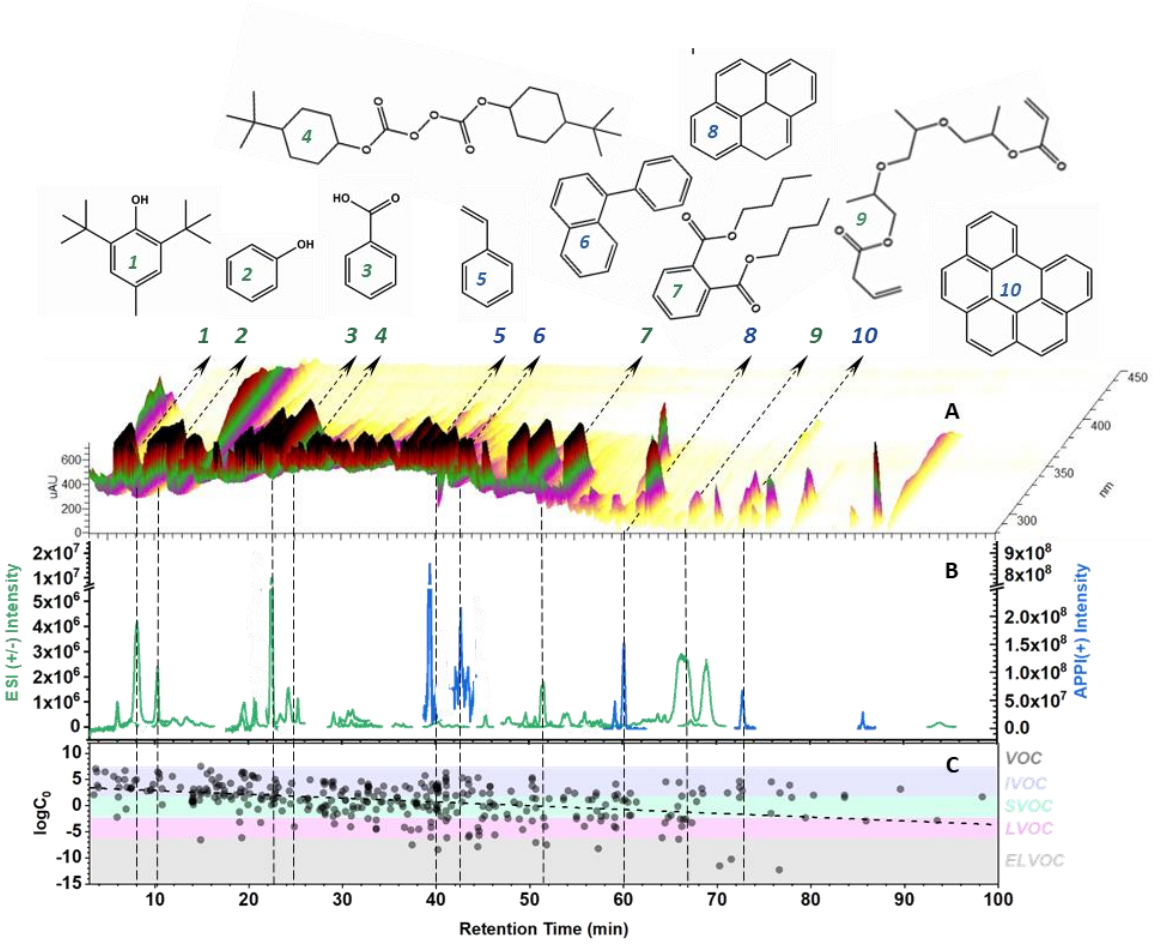

Figure S3. Molecular characteristics of individual components identified in the CIPP steam condensate. A) an HPLC PDA and B) HPLC HRMS (selected ions) chromatograms of the separated solvent-soluble species and C) Estimated volatility ($\log C_0$; μg m^{-3}).

260

Table S3. Summary table of identified molecular components in the X1 waste condensate shown in Figure S3 with corresponding retention time, molecular formula, proposed structure, and relevant notes.

I.D. #	Retention time (min)	Experimental *m/z*	Error (ppm)	Neutral Formula	Proposed Structure	Notes
1	8.14	219.1754 ESI(-)	-0.003	$C_{15}H_{24}O$	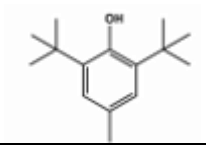	*Name:* butylated hydroxytoluene *Notes:* previously identified[1]
2	10.36	93.0343 ESI(-)	-3.203	C_6H_6O	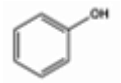	*Name:* phenol *Notes:* oxidized product of styrene
3	21.05	121.0292 ESI(-)	2.574	$C_7H_6O_2$	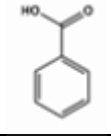	*Name:* benzoic acid *Notes:* oxidized product of styrene
4	24.49	399.2723 ESI(+)	-4.646	$C_{22}H_{38}O_6$	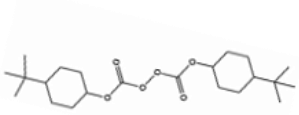	*Name:* di-(4-tert-butylcyclohexyl) peroxy dicarbonate *Notes:* initiator
5	39.41	105.0698 APPI(+)	0.542	C_8H_8	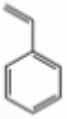	*Name:* styrene *Notes:* resin monomer
6	42.61	205.1015 APPI(+)	-1.526	$C_{16}H_{12}$	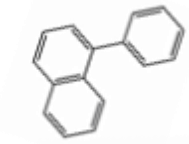	*Name:* phenylnaphthalene *Notes:* PAH byproduct
7	50.7	301.1410 279.1591 ESI(+)	0.033 0.122	$C_{16}H_{22}O_4$	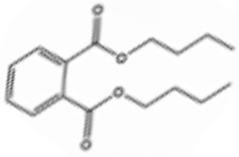	*Name:* dibutyl phthalate *Notes:* phthalate ester
8	60.14	202.0775 APPI(+)	0.950	$C_{16}H_{10}$	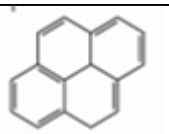	*Name:* pyrene *Notes:* PAH byproduct
9	42.77	301.1646 ESI(+)	-0.050	$C_{15}H_{24}O_6$	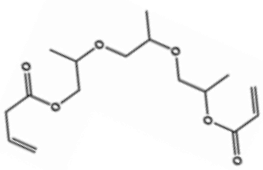	*Name:* tripropylene glycol diacrylate *Notes:* difunctional acrylic monomer

10	72.92	276.0932 APPI(+)	0.551	$C_{22}H_{12}$		*Name:* Benzo[ghi]perylene *Notes:* PAH byproduct

265

Supplementary Note 6: Polymerization and Oligomerization Mechanism

CIPP technology utilizes peroxide initiators for free radical polymerization. At the field sites of this study, both a styrene (vinyl resin) and low-VOC non-styrene (vinyl ester resin) were employed for CIPP manufacture. For each resin type, the polymerization is initiated on the ethylene group of the monomer compound. Scheme S1 shows a peroxide initiator decomposes to form free radicals which break π–bonds in the ethylene group, followed by radical propagation and termination reactions.[13] Previously identified monomers of CIPP composite material include styrene as the main monomer, and additional monomers of ethylene glycol dimethacrylate, methacrylic acid, maleic anhydride, and 2-propenylbenzene.[14–16]

Environmental oligomerization reactions of other coinciding compounds (e.g. aldehydes, ketones, carboxylic acids) also occur in the aqueous droplets (Scheme S2).[17–22] For example, carboxylic acids undergo esterification to form a carbonyl ester oligomer byproduct.[19] Evaporation of water from the microdroplets accelerates these oligomerization processes by confining the reaction volumes, which leads to compositional changes of the organic material in the drying microdroplets.[23,24] The solubility of the organic material is reduced when it undergoes oligomerization, which allows for the formation of EnvNP.[23] These newly formed EnvNP particles do not resemble the intended composition of the CIPP plastic (e.g. polystyrene), therefore their chemical composition differs from those of common microplastic particles.[25]

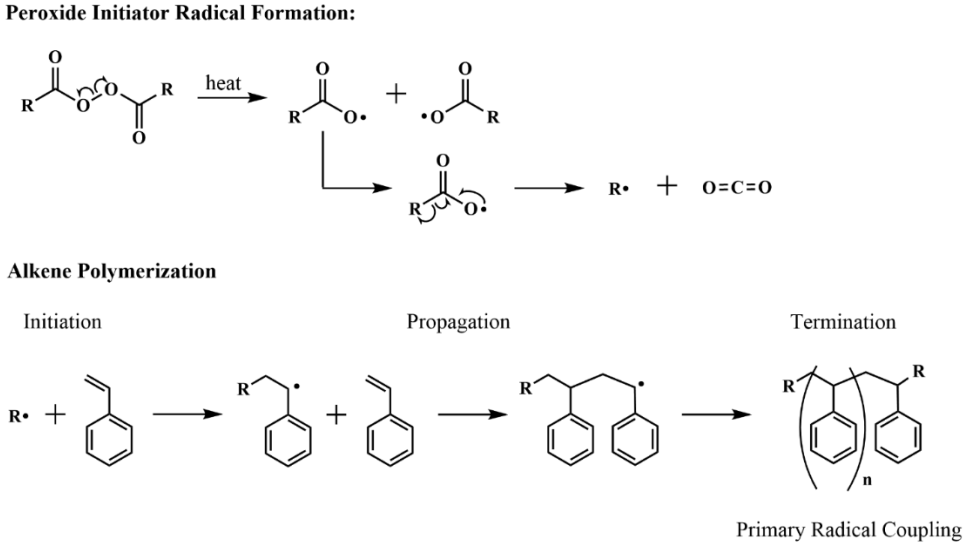

Scheme S1. Polymerization mechanism of styrene with peroxide initiators adapted from Priddy (1994).[13]

Esterification:

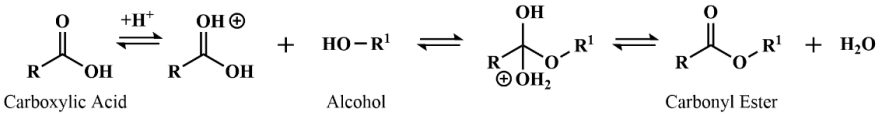

Aldol Condensation:

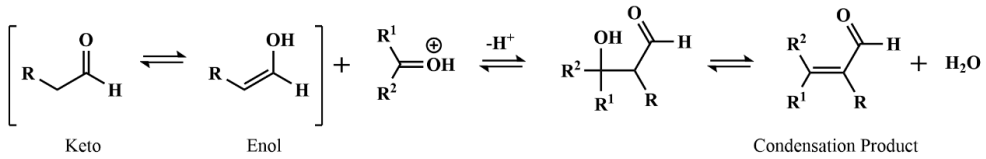

Hemiacetal Formation

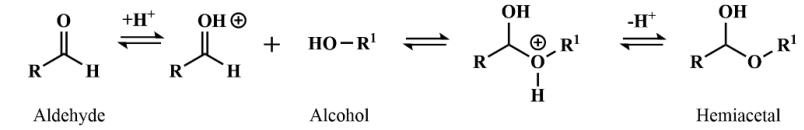

Peroxyhemiacetal Formation

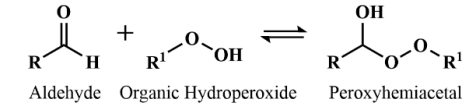

Acetal Formation

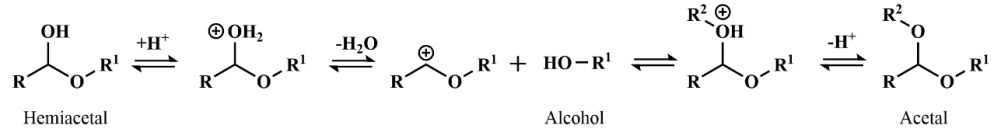

Schiff Base Formation

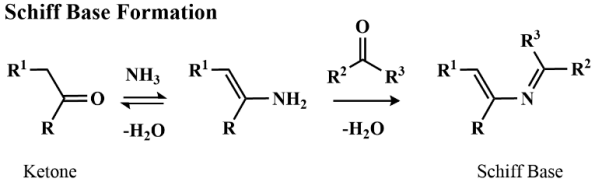

Anionic Oligomerization

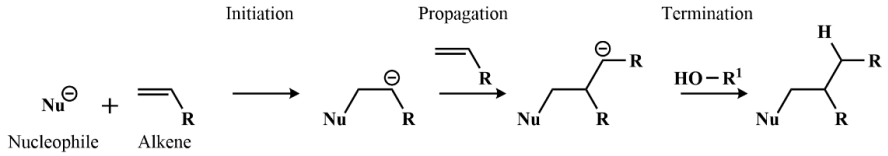

Cationic Oligomerization

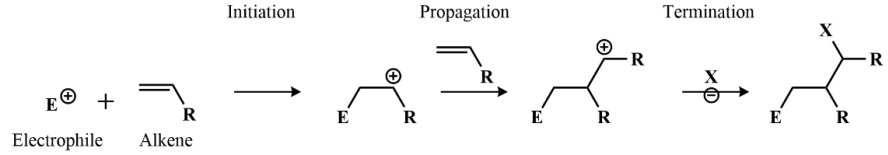

Scheme S2. Plausible formation pathways of oligomers adapted from Kimura (1998), Ziemann (2003), Nguyen et al. (2011), Zhao et al. (2013), Laskin et al. (2014), and Herrmann et al. (2015). [17–22]

Supplementary Note 7: SEM Imaging and Assessment of Particle Viscosity

During collection of airborne particles using an impactor, particles experience deformation of their shape after impact, a behavior affected (between many other factors) by their viscosity.[26–28] Liquid-like particles become flat after colliding with the impactor plate, while highly viscous organic particles retain their spherical shape. Measurements of height (H) and width (W) of particles imaged at tilted angle can be used to estimate particle viscosity based on the H/W ratio values.[29]

Figure S4 shows the height and diameter measurements (obtained with ImageJ software 1.52a, National Institutes of Health) of standard saccharide particles with known viscosities imaged by SEM at tilted 75°. Particulate saccharides with viscosities of $\geq 10^{10}$ Pa s (raffinose, dried at 40% RH)[29] were observed to fall on the 1:1 ratio line, suggesting a spherical (billiard ball) dominant morphology. An H/W ratio of ~1 is expected for highly viscous organic particles as their morphology is preserved. Particles with intermediate viscosities of 10^0-10^5 Pa s (10^0 Pa s: glucose, dried at 76% RH; 10^5 Pa s: glucose, dried at 40% RH)[29] showed H/W ratios of 0.3-0.4, which are representative of particles with dome-like shapes. Particles with water-like viscosities ($\leq 10^{-3}$ Pa s)[29] flatten upon impaction, yielding H/W ratio of ≤0.1.[26,28]

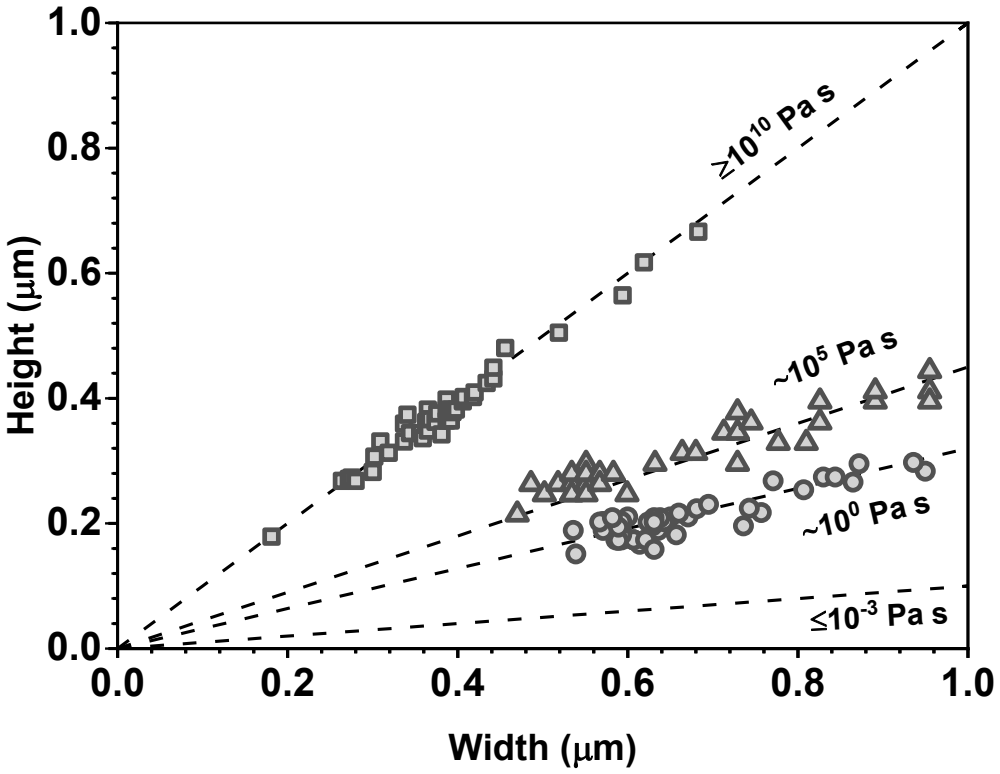

Figure S4. Plot of observed height as a function of particle diameter after impact for individual particles of known viscosity. Dashed lines represent expected trends for highly viscous, spherical (billiard ball-like) particles ($\geq 10^{10}$ Pa s), lower viscosity (low dome) particles (10^{0} – 10^{5} Pa s), and liquid-like particles ($\leq 10^{-3}$ Pa s).

Supplementary Note 8: SERS micro-Spectroscopy of Individual Particles

Molecular characteristics of individual relatively large (>1 μm) particles were investigated using surface enhanced Raman spectroscopy (SERS). Spectra were obtained for particles generated from crushing bulk (lyophilized) residue and for individual particles deposited on substrates. SERS measurements were performed using a confocal Raman microscope.[30] The SERS substrate consisted of a glass substrate sputtered-coated with 50 nm of Au with nanoscale roughness to provide local optical field enhancement to improve Raman sensitivity. The analyte was then deposited on this coated surface and scanned relative to a focused 633 nm HeNe laser to collect single particle hyperspectral Raman images. Acquisition times ranged from 1-10 s depending on signal levels.

Spectral characteristics were identified using the Wiley KnowItAll™ Raman spectral database software and compared to current literature. The X1 site individual particles and lyophilized residue resembled polystyrene (PS) and styrene maleic anhydride (SMA) (Figure 4 and Figure S5). The apparent PS features[31,32] are: stretching modes of aliphatic C-H at 2931 cm^{-1} (asym) and 2868 cm^{-1} (sym), stretching of aromatic C-H at 3075 cm^{-1} and bending at 1435 cm^{-1} and 1154 cm^{-1}, C=C vibration at 1602 cm^{-1}, 'breathing mode' of the aromatic ring at 1000 cm^{-1}, C-C vibration at 614 cm^{-1}. Representative spectra of selected particles from all four samples are presented in Figure S5. The solid lines indicate the major PS features observed in the individual particles. The dashed line indicate additional spectral characteristics specific to poly(styrene maleic anhydride) (SMA) [31,32] of the C=O stretching at 1889 cm^{-1} and 1807 cm^{-1} (sites X1 and X2). The dashed-dotted lines show features of polydimethylsiloxane[31,33] (PDMS) at 1077 cm^{-1} and 2107 cm^{-1} (site X4). The dotted lines indicate peaks at 1528 cm^{-1} and 2024 cm^{-1} characteristic of 2-ethyl-4-methylimidazole[31] (EMD) which is commonly used as a cross-linker for epoxy resins and also as a curing agent (site X2). The particles in the X5 waste condensate were <1 μm, therefore the sensitivity was insufficient to identify spectral features in these particles.

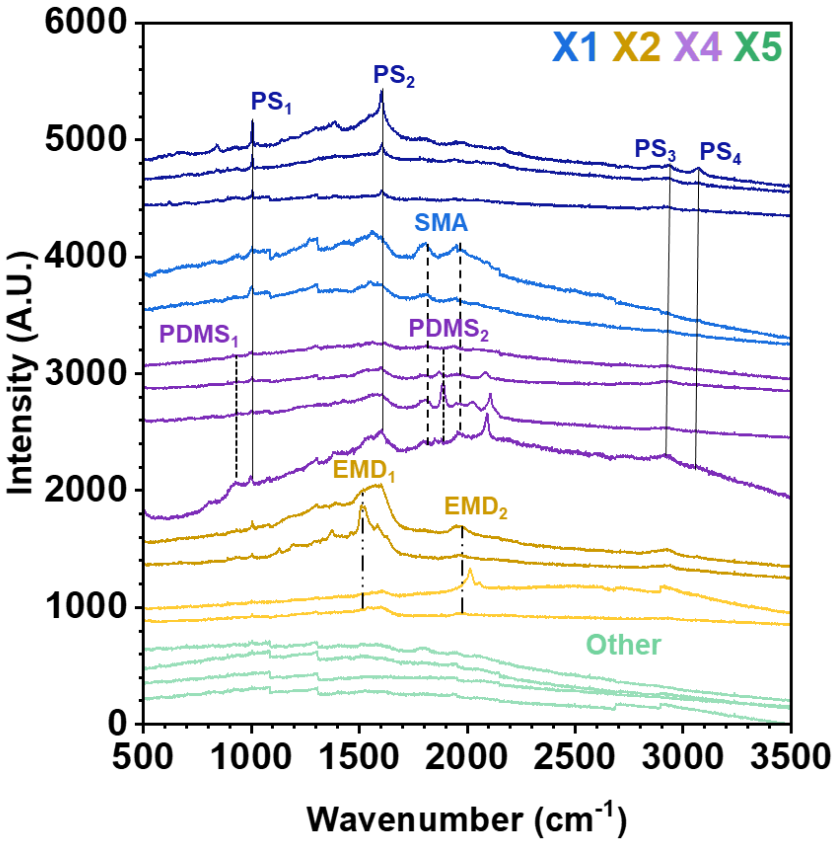

Figure S5. Surface enhanced Raman spectra of individual dry EnvNP particles aerosolized from four samples of CIPP waste condensate. Solid vertical lines indicate the major PS[31,32] features observed for symmetric stretching of the aliphatic C-H at 2868 cm^{-1}, stretching of aromatic C-H at 3075 cm^{-1} and bending at 1435 cm^{-1} and 1154 cm^{-1}, C=C vibration at 1602 cm^{-1}, and 'breathing mode' of the aromatic ring at 1000 cm^{-1}. Dashed lines indicate additional spectral characteristics specific to SMA[31,32] of the C=O stretching at 1889 cm^{-1} and 1807 cm^{-1}. Dotted lines show features of PDMS[31,33] at 1077 cm^{-1} and 2107 cm^{-1}. Dashed-dotted lines indicate peaks at 1528 cm^{-1} and 2024 cm^{-1} characteristic of EMD[31].

Supplementary Note 9: CCSEM-EDX Particle Analysis

The size and elemental composition of individual particles were analyzed using a computer-controlled scanning electron microscope equipped with energy dispersive X-ray spectroscopy operating at the accelerating voltage of 20 kV (CCSEM/EDX; FEI Quanta 3D, EDAX Genesis). During instrument operation, selected fields of view are systematically imaged in search for individual particles. In this work, particles with a diameter greater than >0.1 µm were measured followed by the acquisition of their EDX spectra.[34] The elemental fractions of 14 basic elements (i.e., C, N, O, Na, Mg, Al, Si, P, S, Cl, K, Ca, Mn and Fe) were quantified from EDX spectra. Furthermore, the square root of elemental fractions was utilized in the clustering analysis to allow for a larger weighing of trace elements.[35] Particle lists from all four samples analyzed by CCSEM measurements were combined prior to the application of the *k-means* algorithm.[36] *k-means* clustering is an unsupervised machine learning algorithm with the purpose of grouping different *n* components into *k* clusters based on the nearest mean (i.e., cluster centers or centroids), while minimizing within cluster variances.[36] However, the user must initialize the algorithm by defining the initial number of *k* clusters and allow the algorithm to converge until the assignments of the data sets remains unchanged. Of note, the number of clusters was chosen based on traditional methods for identifying optimal number of *k* clusters such as the elbow method and the silhouette method. In addition, a sophisticated analysis tool, the NbClust function of the R statistical software, was also implemented to identify the best number of *k* clusters based on the "majority rule" of more than 30 indices varying the combinations of the number of clusters, aggregation schemes, and distance measures.[37] Following Figure S6, the calculated optimal number of *k* clusters using elbow, silhouette, and NbClust function were 3, 2, and 3, respectively. As a result, the optimal number of k clusters used for the CCSEM/EDX measurements was identified to be 3.

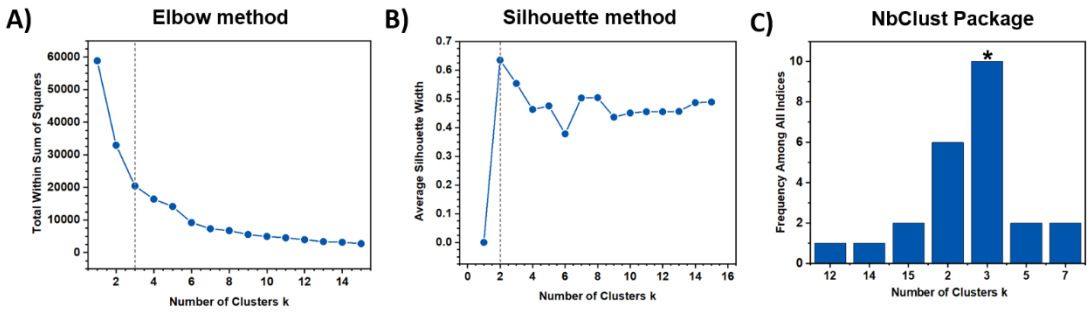

Figure S6. Determining the optimal number of *k*. A) Elbow method; B) Silhouette method; C) NbClust function of R statistical software.

A total of ~11,600 individual particles were analyzed with data generated by EDX analysis providing individual elemental composition. Reported particle size is based on the projected area equivalent diameter (AED, μm). Three major clusters were identified based on the mean elemental contribution: (1) "Inorganic Salt," (2) "Organics," (3) "Mineral Dust," as shown in Figure S7. The mean particle sizes these clusters are well below <1 μm, where "Organics" is the dominant particle-type followed by the "Inorganic Salts" and "Mineral Dust" types which reflect internal mixing of particles with inorganic components. Overall, "Organics" were found to be 75.1% of the total particles analyzed by CCSEM/EDX. Figure S8 shows the individual particle composition as a stacked bar plot with the distribution of the identified particle-types among airborne particles generated from the CIPP waste condensate

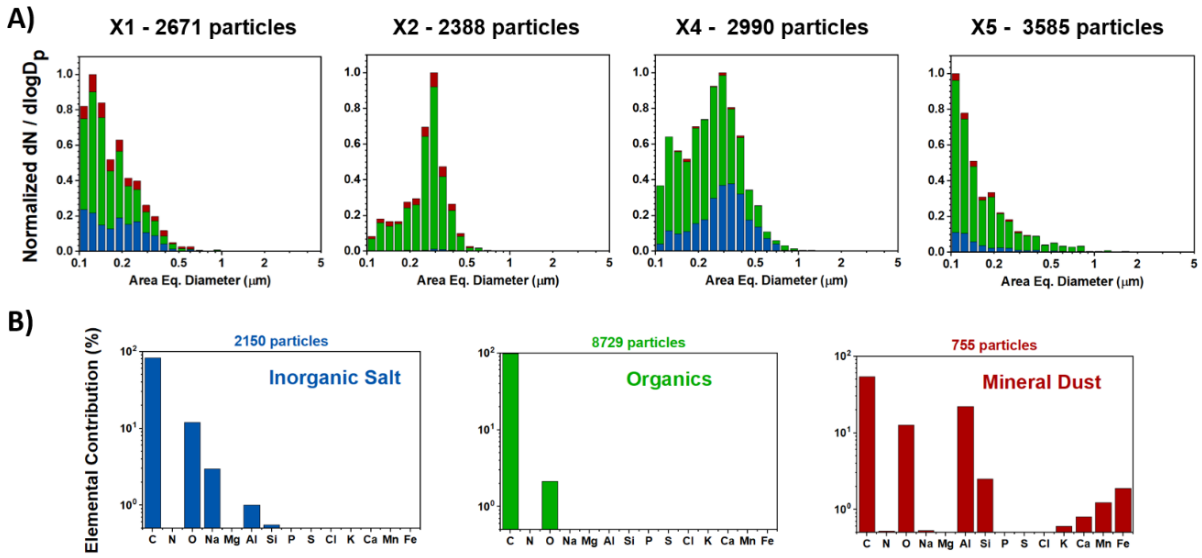

Figure S7. Particle-type population obtained from CCSEM/EDX analysis and identified by *k-means* clustering. A) Normalized particle-type size distributions of shown as a 16 bin/decade histogram representative of particle ensembles aerosolized from each CIPP waste condensate. B) Calculated mean composition of particles corresponding to three major *k* clusters (elemental fractions are plotted in logarithmic scale).

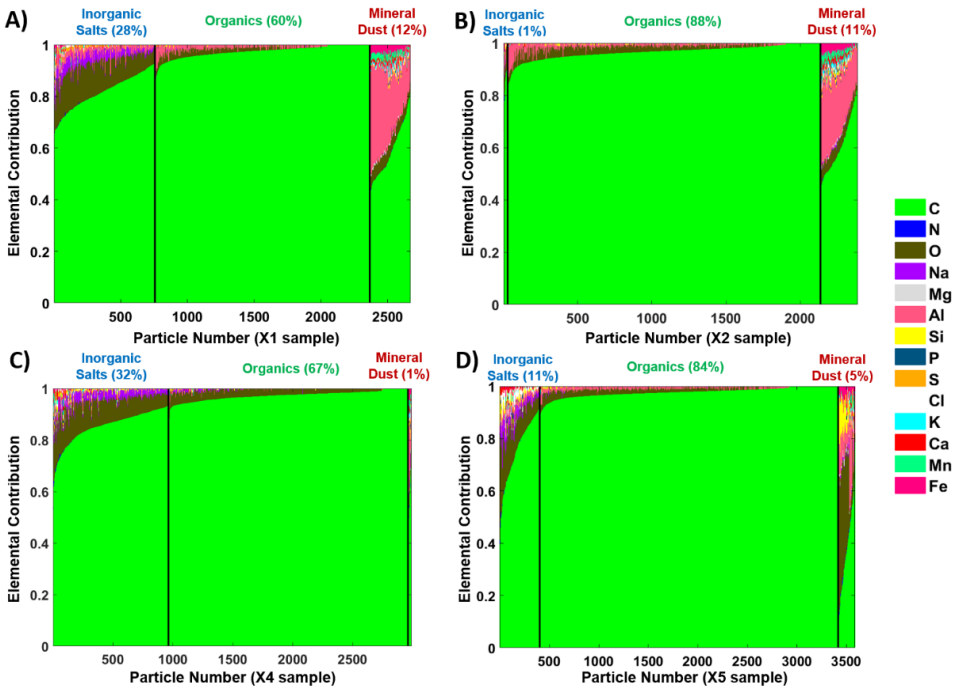

Figure S8. Elemental contribution bar plot of individual particles aerosolized from CIPP waste condensate derived from CCSEM/EDX measurements. The color of each component in the bar indicates the elemental composition of a single particle. The particles are grouped into three distinct clusters identified by *k-means* clustering, separated by the vertical black lines. A) X1 sample; B) X2 sample; C) X4 sample; D) X5 sample.

Supplementary Note 10: Chemical Imaging of Individual EnvNP Particles Using STXM

Scanning Transmission X-ray Microscopy (STXM) coupled with Near Edge X-ray Absorption Fine Structure Spectroscopy (NEXAFS) were used to spatially resolve the chemical bonding and oxidation state of carbon in individual EnvNP particles.[38] The STXM/NEXAFS is a synchrotron based technique where monochromatic X-ray light energy is directed to the STXM beamline and focused using a Fresnel zone plate, where the sample with particles is raster scanned at the focal point.[39] An Order Sorting Aperture (OSA) is placed between the zone plate and sample to filter higher-order diffracted light and allow predominantly first-order diffracted light to be delivered to the sample.[39]

At each X-ray energy, spatially resolved transmission images of the sample are recorded. The transmitted light is then reconstructed into optical density (OD_E) based on the Beer-Lambert's Law with the intensity of transmitted light $I_0(E)$ over areas without particles compared against the transmitted light $I(E)$ recorded through projected region of particles.

$$OD_E = -\ln\left(\frac{I(E)}{I_0(E)}\right) = \mu\rho t \quad \text{(E11)}$$

where μ is the mass absorption coefficient, ρ is the mass density, and t is the thickness of the sample.[40] A series of STXM images is acquired as a function of energy to generate a three-dimensional "stack" data set providing spectral information from individual pixels of detected particles at the carbon absorption edge (~96 energies between 278 to 320 eV, 35 nm spatial resolution, 1 ms dwell time). Figures 5A and S10 illustrate representative NEXAFS spectra of individual EnvNP particles generated from the CIPP waste condensates. Additional STXM/NEXAFS data was acquired in "spectral maps" mode[40] to accumulate greater statistics among analyzed particles by utilizing a faster data acquisition of STXM images at four key energies at 278 eV (pre-edge), 285.4 eV (C=C), 288.5 eV (-COOH), and 320 eV (post-edge) (15x15 μm, 35 nm spatial resolution, 1 ms dwell time) as shown in Figure 5B. For data analysis, we employed established image processing and spectral analysis methods as reported in our previous studies.[26,40–43] Briefly, pixel resolved components among individual particles were classified based on three defined thresholds. "Organic Carbon" (OC) is classified as the difference between the OD of the carboxylic acid peak (288.5 eV) and the carbon pre-edge peak (278 eV) is greater than 0 (i.e., $OD_{288.5eV} - OD_{278eV} > 0$). "Elemental Carbon/Soot" (EC) regions are defined

as the ratio of the intensity of sp^2 C=C peak (285.4 eV) to the total carbon (TC) (i.e., $OD_{320eV} - OD_{278eV}$) ratioed to the highly oriented pyrolytic graphite (HOPG) standard as defined below[44]:

$$\frac{OD_{285.4\ eV}^{Sample}}{OD_{320\ eV}^{Sample} - OD_{278\ eV}^{Sample}} \cdot \frac{OD_{320\ eV}^{HOPG} - OD_{278\ eV}^{HOPG}}{OD_{285.4\ eV}^{HOPG}} > 0.35 \quad \text{(E1)}$$

This definition considers the sp^2 bonding of carbon being analogous to a highly graphitic-like structure.[44] Finally, "Inorganics" (IN) regions are those where $OD_{278eV}/OD_{320eV} > 0.5$. Approximately 336 particles were analyzed across all four samples.

The assessment of particle viscosity can be additionally derived from STXM/NEXAFS measurements. Particles deform upon impact with the substrate, as described in Supplementary Note 6. The extent of deformation depends on the particle viscosity, which can be inferred from the total carbon absorption (TCA) measured as the difference between OD at the post-edge and at the pre-edge energies:[27]

$$TCA = OD_{320\ eV} - OD_{278\ eV} \quad \text{(E2)}$$

Assuming similar μ and ρ among the particle population, we can relate the measured *TCA* to the height of the impacted particle since it is proportional to extent at which the light traverse through the particle.[38] Therefore, larger *TCA* values per unit of particle 2D-projected area (TCA/D_p) indicate tall viscous particles. Based on our previous studies values of $TCA/D_p > 0.7$ are those that denote either *spherical* or *tall dome-like* particles.[26,27,45] Figure S9 compares the averaged NEXAFS spectra of *spherical* EnvNP particles ($TCA/D_p > 0.7$, shown in Figure 5 of the manuscript) to the NEXAFS spectra of common polymers.[46,47] Notably, spectra of the EnvNP particles do not precisely match those of the listed polymer standards. However, the EnvNP spectra still share absorbance features that could potentially be a combination of various polymer components, which is consistent with the assumption that these particles are generated in an irregular polymerization process from residues of a very complex material used for CIPP installation.

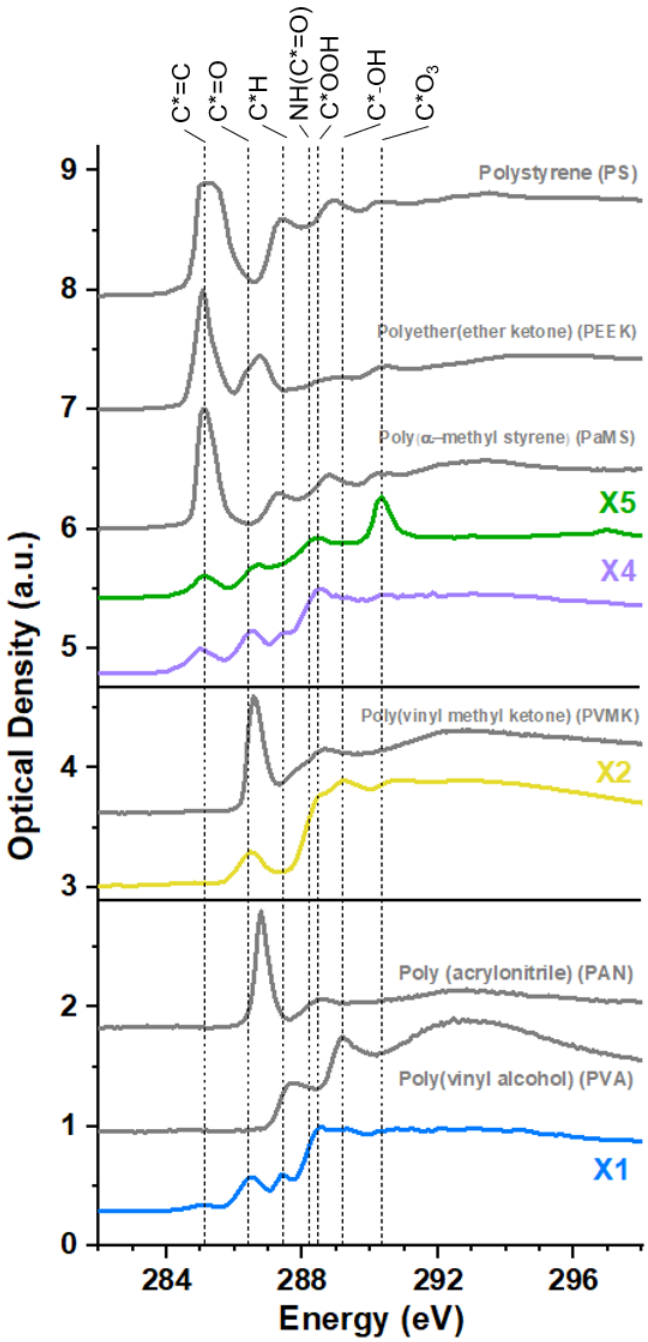

Figure S9. Average carbon K-edge NEXAFS spectra of *spherical* EnvNP particles (Figure 5 of the manuscript) generated from each of the CIPP waste condensates (colored lines), compared against thin film standards of common polymers[46] (grey lines). Dashed grey lines correspond to carbon K-edge spectral features: 285.4 eV (C*=C), 286.7 eV (C*=O), 287.7 eV (C*–H), 288.3 eV (R-NH(C*=O)R), 288.5 eV (R(C*=O)OH), 289.5 eV (RC*–OH), 290.0 eV (C edge step), and 290.4 eV (C*O3).

Figure S10 shows the NEXAFS spectra corresponding to *flat-like* particles with TCA/D_p << 0.7. Their spectral features are overall consistent with their *spherical* counterparts from the same samples, suggesting that particle polymerization does not occur uniformly.

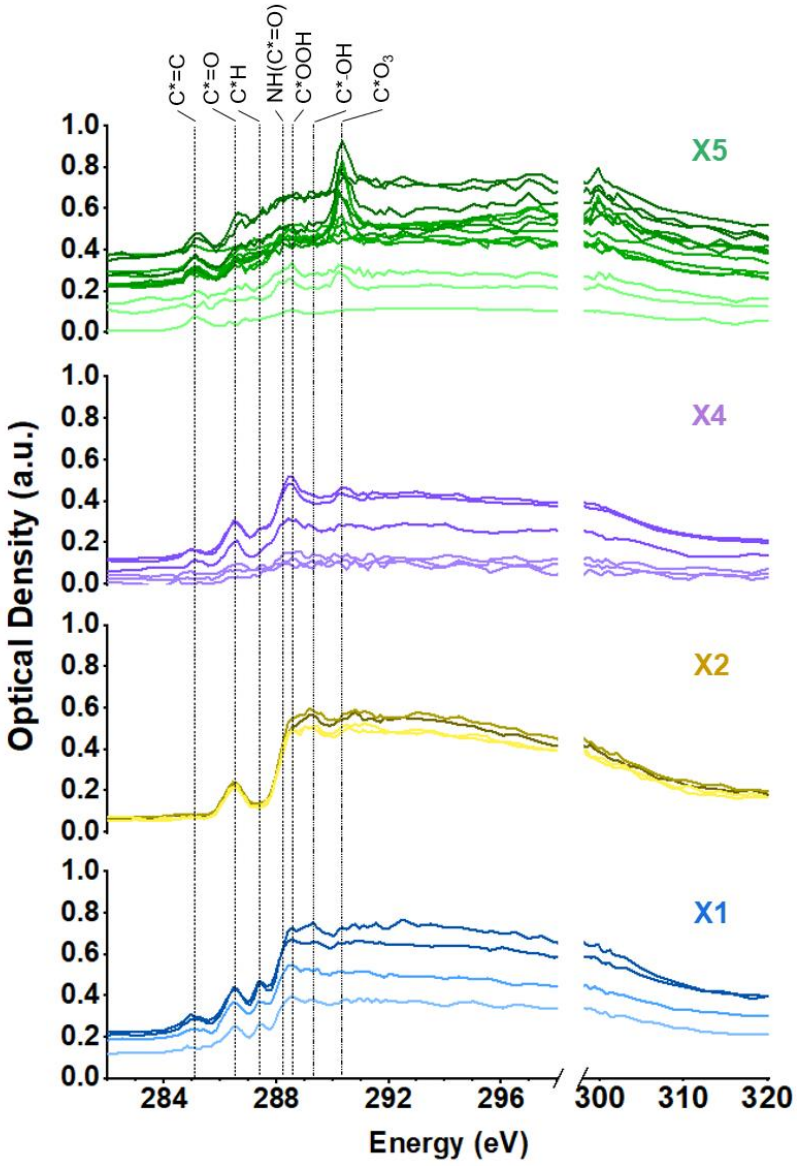

Figure S10. STXM/NEXAFS spectra of individual *flat-like* particles characterized by TCA/D_p < 0.7 values. Dashed grey lines correspond to carbon K-edge spectral features: 285.4 eV (C*=C), 286.7 eV (C*=O), 287.7 eV (C*–H), 288.3 eV (R-NH(C*=O)R), 288.5 eV (R(C*=O)OH), 289.5 eV (RC*–OH), 290.0 eV (C edge step), and 290.4 eV (C*O3).

The organic volume fractions (OVF) of individual particles were calculated from STXM spectral maps following method described in Fraund et al. (2019).[42] Briefly, the optical density (OD) at the pre-edge (278 eV) is related to the IN mass while the post-edge (320 eV) is correlated to the total mass of the IN and OC components. The OD values at these energies depend on OC and IN components according to the equations introduced in previous works:[42,48]

$$OD_{278} = \mu_{278}^{IN} \rho^{IN} t^{IN} + \mu_{278}^{OC} \rho^{OC} t^{OC} \quad \text{(E3)}$$

$$OD_{320} = \mu_{320}^{IN} \rho^{IN} t^{IN} + \mu_{320}^{OC} \rho^{OC} t^{OC} \quad \text{(E4)}$$

Based on this relationship, we can express the equations to solve for the optical thickness of IN and OC assuming values for the μ and ρ for both OC and IN.[42] OVF can then be calculated at each pixel of the particle image based on the ratio of the optical thickness of the organic constituent (t^{OC}) to the total optical thickness ($t^{OC} + t^{IN}$) as shown in Figure 5C and 5D. This approach for determining OVF is dependent on the assumption used for the organic and inorganic constituents[49] as it slightly affects the values of both μ and ρ. For this work, we modeled the inorganic fraction as $(NH_4)SO_4$ while the organic fraction was approximated as a single component composed of sucrose, glucose, adipic acid, or oxalic acid. These organics were chosen based on previously reported literature for STXM-derived OVF calculations.[42,49,50] Figure 5D shows the size-resolved average OVF values with approximately a 5-10% difference in OVF when varying the organic component among the four species.

Supplementary Note 11: TEM images showing changes in EnvNP particles after heating.

Transmission electron microscopy (TEM) images were obtained with an FEI Titan environmental transmission electron microscope (FEI, Hillsboro, OR) coupled with a single tilt heating holder operated at 300 kV. Each sample was heated for 5 minutes using a heating stage at each set temperature and images were acquired after the sample was cooled down back to 25°C.

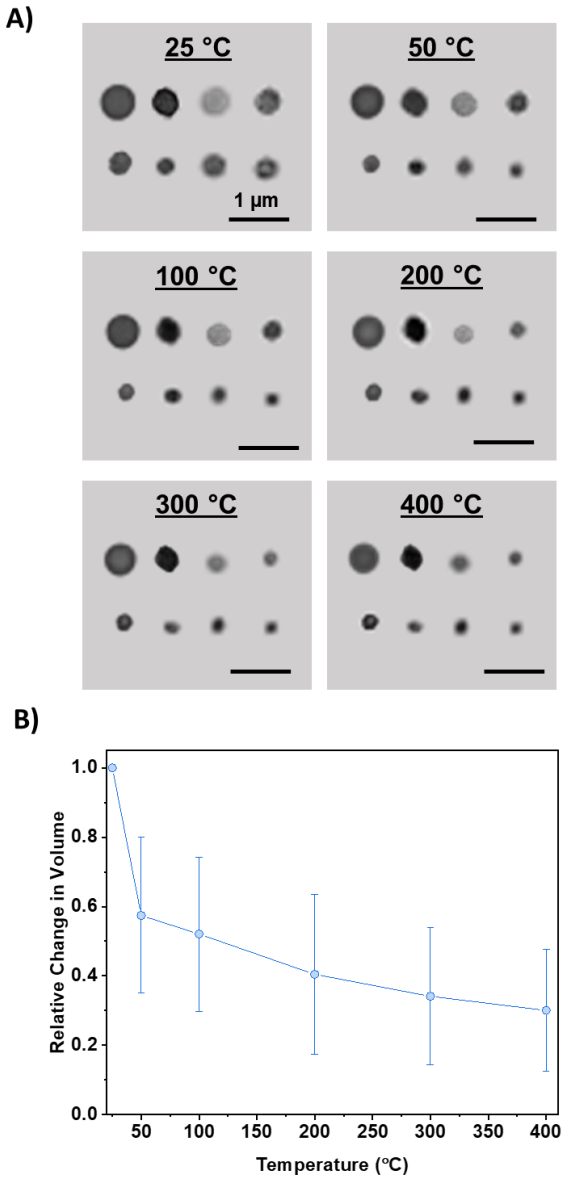

Figure S11. A) Collages of individual EnvNP particles as a function of heating temperature. The scale bar in each image is 1 µm. B) Averaged relative changes in the volume of particles as a

function of heating temperature. Particle volumes were calculated using area equivalent diameters derived from 2D particle projection areas.

Supplementary Note 12: Visual Observation of the Condensed-Phase White Powder Deposits at the Field Cite of CIPP Installation.

Occurrence of white chemical plumes and their movement due to local environmental conditions and passage by nearby vehicles were video recorded at the CIPP installation cites (Videos S1-S3 in Sendesi et al 2017).[1] Figure S11 also illustrates a photograph from the site showing deposits of white powder on surface of the leaves from trees nearby. Chemical composition of this white material was unidentifiable by monitoring equipment deployed at the site.

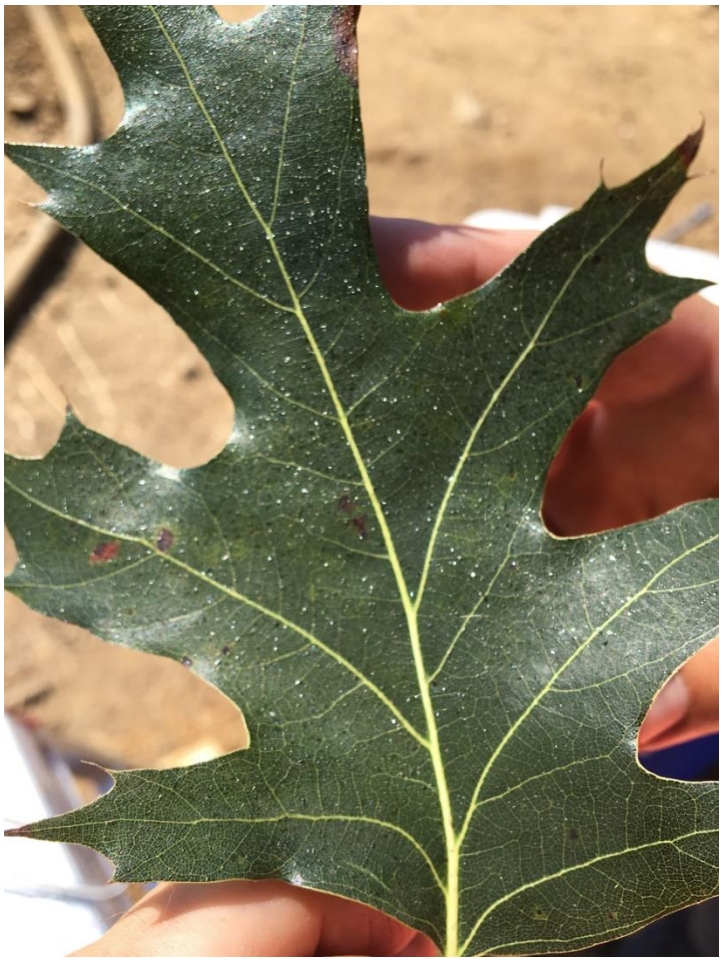

Figure S12. Photograph from an CIPP installation cite of an oak tree leaf directly above the exhaust hose shows deposits of white powder particles, which were absent from unexposed leaves. A video of the discharged waste plume adjacent to the oak tree is included as Supplementary Video S1.

Supplementary Note 13: Summary of the public records indicating total mass of resin materials used in selected CIPP projects performed in U.S. urban areas and the experimentally determined mass of resin lost into atmosphere during CIPP manufacture are compiled in the SI file (Table S2 and references therein) of *Teimouri Sendesi et al*, 2020.[16]

References

(1) Teimouri Sendesi, S. M.; Ra, K.; Conkling, E. N.; Boor, B. E.; Nuruddin, Md.; Howarter, J. A.; Youngblood, J. P.; Kobos, L. M.; Shannahan, J. H.; Jafvert, C. T.; Whelton, A. J. Worksite Chemical Air Emissions and Worker Exposure during Sanitary Sewer and Stormwater Pipe Rehabilitation Using Cured-in-Place-Pipe (CIPP). *Environ. Sci. Technol. Lett.* **2017**, *4* (8), 325–333. https://doi.org/10.1021/acs.estlett.7b00237.

(2) Ra, K.; Teimouri Sendesi, S. M.; Nuruddin, Md.; Zyaykina, N. N.; Conkling, E. N.; Boor, B. E.; Jafvert, C. T.; Howarter, J. A.; Youngblood, J. P.; Whelton, A. J. Considerations for Emission Monitoring and Liner Analysis of Thermally Manufactured Sewer Cured-in-Place-Pipes (CIPP). *J. Hazard. Mater.* **2019**, *371*, 540–549. https://doi.org/10.1016/j.jhazmat.2019.02.097.

(3) L040-TNVG-33: MSDS No. 14764V2; AOC, LLC: Collierville, TN, August 30, 2012.

(4) United States Environmental Protection Agency (USEPA). Method 415.1. Organic Carbon, Total (Combustion or Oxidation), 1974.

(5) Anger, P. M.; von der Esch, E.; Baumann, T.; Elsner, M.; Niessner, R.; Ivleva, N. P. Raman Microspectroscopy as a Tool for Microplastic Particle Analysis. *TrAC Trends Anal. Chem.* **2018**, *109*, 214–226. https://doi.org/10.1016/j.trac.2018.10.010.

(6) Hugall, J. T.; Baumberg, J. J. Demonstrating Photoluminescence from Au Is Electronic Inelastic Light Scattering of a Plasmonic Metal: The Origin of SERS Backgrounds. *Nano Lett.* **2015**, *15* (4), 2600–2604. https://doi.org/10.1021/acs.nanolett.5b00146.

(7) Lin, P.; Bluvshtein, N.; Rudich, Y.; Nizkorodov, S. A.; Laskin, J.; Laskin, A. Molecular Chemistry of Atmospheric Brown Carbon Inferred from a Nationwide Biomass Burning Event. *Environ. Sci. Technol.* **2017**, *51* (20), 11561–11570. https://doi.org/10.1021/acs.est.7b02276.

(8) Lin, P.; Fleming, L. T.; Nizkorodov, S. A.; Laskin, J.; Laskin, A. Comprehensive Molecular Characterization of Atmospheric Brown Carbon by High Resolution Mass Spectrometry with Electrospray and Atmospheric Pressure Photoionization. *Anal. Chem.* **2018**, *90* (21), 12493–12502. https://doi.org/10.1021/acs.analchem.8b02177.

(9) Phenomenex Inc. The Ultimate Guide to Reversed Phase HPLC/UHPLC Selectivity, 2013.

(10) Hettiyadura, A. P. S.; Garcia, V.; Li, C.; West, C. P.; Tomlin, J.; He, Q.; Rudich, Y.; Laskin, A. Chemical Composition and Molecular-Specific Optical Properties of Atmospheric Brown Carbon Associated with Biomass Burning. *Environ. Sci. Technol.* **2021**, *55* (4), 2511–2521. https://doi.org/10.1021/acs.est.0c05883.

(11) Li, Y.; Pöschl, U.; Shiraiwa, M. Molecular Corridors and Parameterizations of Volatility in the Chemical Evolution of Organic Aerosols. *Atmospheric Chem. Phys.* **2016**, *16* (5), 3327–3344. https://doi.org/10.5194/acp-16-3327-2016.

(12) Donahue, N. M.; Epstein, S. A.; Pandis, S. N.; Robinson, A. L. A Two-Dimensional Volatility Basis Set: 1. Organic-Aerosol Mixing Thermodynamics. *Atmospheric Chem. Phys.* **2011**, *11* (7), 3303–3318. https://doi.org/10.5194/acp-11-3303-2011.

(13) Priddy, D. B. Recent Advances in Styrene Polymerization. In *Advances in Polymer Science*; Springer-Verlag Berlin Heidelberg, 1994; Vol. 111, pp 67–114.

(14) Noh, Y.; Odimayomi, T.; Teimouri Sendesi, S. M.; Youngblood, J. P.; Whelton, A. J. Environmental and Human Health Risks of Plastic Composites Can Be Reduced by

Optimizing Manufacturing Conditions. *J. Clean. Prod.* **2022**, *356*, 131803. https://doi.org/10.1016/j.jclepro.2022.131803.
(15) Teimouri Sendesi, S. M.; Ra, K.; Conkling, E. N.; Boor, B. E.; Nuruddin, Md.; Howarter, J. A.; Youngblood, J. P.; Kobos, L. M.; Shannahan, J. H.; Jafvert, C. T.; Whelton, A. J. Worksite Chemical Air Emissions and Worker Exposure during Sanitary Sewer and Stormwater Pipe Rehabilitation Using Cured-in-Place-Pipe (CIPP). *Environ. Sci. Technol. Lett.* **2017**, *4* (8), 325–333. https://doi.org/10.1021/acs.estlett.7b00237.
(16) Teimouri Sendesi, S. M.; Noh, Y.; Nuruddin, M.; Boor, B. E.; Howarter, J. A.; Youngblood, J. P.; Jafvert, C. T.; Whelton, A. J. An Emerging Mobile Air Pollution Source: Outdoor Plastic Liner Manufacturing Sites Discharge VOCs into Urban and Rural Areas. *Environ. Sci. Process. Impacts* **2020**, *22* (9), 1828–1841. https://doi.org/10.1039/D0EM00190B.
(17) Kimura, H. A Simple Method for the Anionic Polymerization of α-Carbonyl Acids in Water. *J. Polym. Sci. Part Polym. Chem.* **1998**, *36* (1), 189–193. https://doi.org/10.1002/(SICI)1099-0518(19980115)36:1<189::AID-POLA23>3.0.CO;2-E.
(18) Ziemann, P. J. Formation of Alkoxyhydroperoxy Aldehydes and Cyclic Peroxyhemiacetals from Reactions of Cyclic Alkenes with O3 in the Presence of Alcohols. *J. Phys. Chem. A* **2003**, *107* (12), 2048–2060.
(19) Nguyen, T. B.; Roach, P. J.; Laskin, J.; Laskin, A.; Nizkorodov, S. A. Effect of Humidity on the Composition of Isoprene Photooxidation Secondary Organic Aerosol. *Atmospheric Chem. Phys.* **2011**, *11* (14), 6931–6944. https://doi.org/10.5194/acp-11-6931-2011.
(20) Zhao, R.; Lee, A. K. Y.; Soong, R.; Simpson, A. J.; Abbatt, J. P. D. Formation of Aqueous-Phase α-Hydroxyhydroperoxides (α-HHP): Potential Atmospheric Impacts. *Atmospheric Chem. Phys.* **2013**, *13* (12), 5857–5872. https://doi.org/10.5194/acp-13-5857-2013.
(21) Herrmann, H.; Schaefer, T.; Tilgner, A.; Styler, S. A.; Weller, C.; Teich, M.; Otto, T. Tropospheric Aqueous-Phase Chemistry: Kinetics, Mechanisms, and Its Coupling to a Changing Gas Phase. *Chem. Rev.* **2015**, *115* (10), 4259–4334. https://doi.org/10.1021/cr500447k.
(22) Laskin, J.; Laskin, A.; Nizkorodov, S. A.; Roach, P.; Eckert, P.; Gilles, M. K.; Wang, B.; Lee, H. J. (Julie); Hu, Q. Molecular Selectivity of Brown Carbon Chromophores. *Environ. Sci. Technol.* **2014**, *48* (20), 12047–12055. https://doi.org/10.1021/es503432r.
(23) Nguyen, T. B.; Lee, P. B.; Updyke, K. M.; Bones, D. L.; Laskin, J.; Laskin, A.; Nizkorodov, S. A. Formation of Nitrogen- and Sulfur-Containing Light-Absorbing Compounds Accelerated by Evaporation of Water from Secondary Organic Aerosols: BROWN CARBON FROM DROPLET EVAPORATION. *J. Geophys. Res. Atmospheres* **2012**, *117* (D1), n/a-n/a. https://doi.org/10.1029/2011JD016944.
(24) Petters, S. S.; Hilditch, T. G.; Tomaz, S.; Miles, R. E. H.; Reid, J. P.; Turpin, B. J. Volatility Change during Droplet Evaporation of Pyruvic Acid. *ACS Earth Space Chem.* **2020**, *4* (5), 741–749. https://doi.org/10.1021/acsearthspacechem.0c00044.
(25) Gigault, J.; El Hadri, H.; Nguyen, B.; Grassl, B.; Rowenczyk, L.; Tufenkji, N.; Feng, S.; Wiesner, M. Nanoplastics Are Neither Microplastics nor Engineered Nanoparticles. *Nat. Nanotechnol.* **2021**, *16* (5), 501–507. https://doi.org/10.1038/s41565-021-00886-4.
(26) Tomlin, J. M.; Jankowski, K. A.; Rivera-Adorno, F. A.; Fraund, M.; China, S.; Stirm, B. H.; Kaeser, R.; Eakins, G. S.; Moffet, R. C.; Shepson, P. B.; Laskin, A. Chemical Imaging

of Fine Mode Atmospheric Particles Collected from a Research Aircraft over Agricultural Fields. *ACS Earth Space Chem.* **2020**, *4* (11), 2171–2184. https://doi.org/10.1021/acsearthspacechem.0c00172.

(27) O'Brien, R. E.; Neu, A.; Epstein, S. A.; MacMillan, A. C.; Wang, B.; Kelly, S. T.; Nizkorodov, S. A.; Laskin, A.; Moffet, R. C.; Gilles, M. K. Physical Properties of Ambient and Laboratory-Generated Secondary Organic Aerosol: PHYSICAL PROPERTIES OF ORGANIC AEROSOL. *Geophys. Res. Lett.* **2014**, *41* (12), 4347–4353. https://doi.org/10.1002/2014GL060219.

(28) Wang, B.; Harder, T. H.; Kelly, S. T.; Piens, D. S.; China, S.; Kovarik, L.; Keiluweit, M.; Arey, B. W.; Gilles, M. K.; Laskin, A. Airborne Soil Organic Particles Generated by Precipitation. *Nat. Geosci.* **2016**, *9* (6), 433–437. https://doi.org/10.1038/ngeo2705.

(29) Reid, J. P.; Bertram, A. K.; Topping, D. O.; Laskin, A.; Martin, S. T.; Petters, M. D.; Pope, F. D.; Rovelli, G. The Viscosity of Atmospherically Relevant Organic Particles. *Nat. Commun.* **2018**, *9* (1), 956. https://doi.org/10.1038/s41467-018-03027-z.

(30) Perez Beltran, S.; Cao, X.; Zhang, J.-G.; El-Khoury, P. Z.; Balbuena, P. B. Influence of Diluent Concentration in Localized High Concentration Electrolytes: Elucidation of Hidden Diluent-Li^+ Interactions and Li^+ Transport Mechanism. *J. Mater. Chem. A* **2021**, *9* (32), 17459–17473. https://doi.org/10.1039/D1TA04737J.

(31) Wiley Science Solutions. *KnowItAll*.

(32) Schoukens, G.; Martins, J.; Samyn, P. Insights in the Molecular Structure of Low- and High-Molecular Weight Poly(Styrene-Maleic Anhydride) from Vibrational and Resonance Spectroscopy. *Polymer* **2013**, *54* (1), 349–362. https://doi.org/10.1016/j.polymer.2012.11.032.

(33) Cai, D.; Neyer, A.; Kuckuk, R.; Heise, H. M. Raman, Mid-Infrared, near-Infrared and Ultraviolet–Visible Spectroscopy of PDMS Silicone Rubber for Characterization of Polymer Optical Waveguide Materials. *J. Mol. Struct.* **2010**, *976* (1–3), 274–281. https://doi.org/10.1016/j.molstruc.2010.03.054.

(34) Laskin, A. Heterogeneous Chemistry of Individual Mineral Dust Particles with Nitric Acid: A Combined CCSEM/EDX, ESEM, and ICP-MS Study. *J. Geophys. Res.* **2005**, *110* (D10), D10208. https://doi.org/10.1029/2004JD005206.

(35) Rebotier, T. P.; Prather, K. A. Aerosol Time-of-Flight Mass Spectrometry Data Analysis: A Benchmark of Clustering Algorithms. *Anal. Chim. Acta* **2007**, *585* (1), 38–54. https://doi.org/10.1016/j.aca.2006.12.009.

(36) Hartigan, J. A.; Wong, M. A. Algorithm AS 136: A K-Means Clustering Algorithm. *Appl. Stat.* **1979**, *28* (1), 100. https://doi.org/10.2307/2346830.

(37) Charrad, M.; Ghazzali, N.; Boiteau, V.; Niknafs, A. NbClust: An R Package for Determining the Relevant Number of Clusters in a Data Set. *J. Stat. Softw.* **2014**, *61* (6). https://doi.org/10.18637/jss.v061.i06.

(38) Moffet, R. C.; Tivanski, A. V.; Gilles, M. K. Scanning Transmission X-Ray Microscopy: Applications in Atmospheric Aerosol Research. **2010**.

(39) Kilcoyne, A. L. D.; Tyliszczak, T.; Steele, W. F.; Fakra, S.; Hitchcock, P.; Franck, K.; Anderson, E.; Harteneck, B.; Rightor, E. G.; Mitchell, G. E.; Hitchcock, A. P.; Yang, L.; Warwick, T.; Ade, H. Interferometer-Controlled Scanning Transmission X-Ray Microscopes at the Advanced Light Source. *J. Synchrotron Radiat.* **2003**, *10* (2), 125–136. https://doi.org/10.1107/S0909049502017739.

(40) Moffet, R. C.; Henn, T.; Laskin, A.; Gilles, M. K. Automated Chemical Analysis of Internally Mixed Aerosol Particles Using X-Ray Spectromicroscopy at the Carbon K-Edge †. *Anal. Chem.* **2010**, *82* (19), 7906–7914. https://doi.org/10.1021/ac1012909.

(41) Moffet, R. C.; O'Brien, R. E.; Alpert, P. A.; Kelly, S. T.; Pham, D. Q.; Gilles, M. K.; Knopf, D. A.; Laskin, A. Morphology and Mixing of Black Carbon Particles Collected in Central California during the CARES Field Study. *Atmospheric Chem. Phys.* **2016**, *16* (22), 14515–14525. https://doi.org/10.5194/acp-16-14515-2016.

(42) Fraund, M.; Park, T.; Yao, L.; Bonanno, D.; Pham, D. Q.; Moffet, R. C. Quantitative Capabilities of STXM to Measure Spatially Resolved Organic Volume Fractions of Mixed Organic ⁄ Inorganic Particles. *Atmospheric Meas. Tech.* **2019**, *12* (3), 1619–1633. https://doi.org/10.5194/amt-12-1619-2019.

(43) Moffet, R. C.; Rödel, T. C.; Kelly, S. T.; Yu, X. Y.; Carroll, G. T.; Fast, J.; Zaveri, R. A.; Laskin, A.; Gilles, M. K. Spectro-Microscopic Measurements of Carbonaceous Aerosol Aging in Central California. *Atmospheric Chem. Phys.* **2013**, *13* (20), 10445–10459. https://doi.org/10.5194/acp-13-10445-2013.

(44) Hopkins, R. J.; Tivanski, A. V.; Marten, B. D.; Gilles, M. K. Chemical Bonding and Structure of Black Carbon Reference Materials and Individual Carbonaceous Atmospheric Aerosols. *J. Aerosol Sci.* **2007**, *38* (6), 573–591. https://doi.org/10.1016/j.jaerosci.2007.03.009.

(45) Wang, B.; Harder, T. H.; Kelly, S. T.; Piens, D. S.; China, S.; Kovarik, L.; Keiluweit, M.; Arey, B. W.; Gilles, M. K.; Laskin, A. Airborne Soil Organic Particles Generated by Precipitation. *Nat. Geosci.* **2016**, *9* (6), 433–437. https://doi.org/10.1038/ngeo2705.

(46) Dhez, O.; Ade, H.; Urquhart, S. G. Calibrated NEXAFS Spectra of Some Common Polymers. *J. Electron Spectrosc. Relat. Phenom.* **2003**, *128* (1), 85–96.

(47) Walsh, T. The Plastic Piping Industry in North America. In *Applied Plastics Engineering Handbook*; Elsevier, 2011; pp 585–602. https://doi.org/10.1016/B978-1-4377-3514-7.10034-0.

(48) O'Brien, R. E.; Wang, B.; Laskin, A.; Riemer, N.; West, M.; Zhang, Q.; Sun, Y.; Yu, X.; Alpert, P.; Knopf, D. A.; Gilles, M. K.; Moffet, R. C. Chemical Imaging of Ambient Aerosol Particles: Observational Constraints on Mixing State Parameterization. *J. Geophys. Res. Atmospheres* **2015**, *120* (18), 9591–9605. https://doi.org/10.1002/2015JD023480.

(49) Tomlin, J. M.; Jankowski, K. A.; Veghte, D. P.; China, S.; Wang, P.; Fraund, M.; Weis, J.; Zheng, G.; Wang, Y.; Rivera-Adorno, F.; Raveh-Rubin, S.; Knopf, D. A.; Wang, J.; Gilles, M. K.; Moffet, R. C.; Laskin, A. *Impact of Dry Intrusion Events on Composition and Mixing State of Particles During Winter ACE-ENA Study*; preprint; Aerosols/Field Measurements/Troposphere/Chemistry (chemical composition and reactions), 2021. https://doi.org/10.5194/acp-2021-590.

(50) Pham, D. Q.; O'Brien, R.; Fraund, M.; Bonanno, D.; Laskina, O.; Beall, C.; Moore, K. A.; Forestieri, S.; Wang, X.; Lee, C.; Sultana, C.; Grassian, V.; Cappa, C. D.; Prather, K. A.; Moffet, R. C. Biological Impacts on Carbon Speciation and Morphology of Sea Spray Aerosol. *ACS Earth Space Chem.* **2017**, *1* (9), 551–561. https://doi.org/10.1021/acsearthspacechem.7b00069.